

Highly Productive C₃H₄/C₃H₆ Trace Separation by a Packing Polymorph of a Layered Hybrid Ultramicroporous Material

Mei-Yan Gao, Andrey A. Bezrukov, Bai-Qiao Song, Meng He, Sousa Javan Nikkiah, Shi-Qiang Wang, Naveen Kumar, Shaza Darwish, Debobroto Sensharma, Chenghua Deng, Jiangnan Li, Lunjie Liu, Rajamani Krishna, Matthias Vandichel, Sihai Yang, and Michael J. Zaworotko*



Cite This: *J. Am. Chem. Soc.* 2023, 145, 11837–11845



Read Online

ACCESS |



Metrics & More

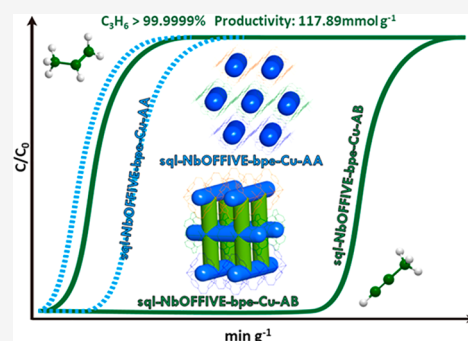


Article Recommendations



Supporting Information

ABSTRACT: Ultramicroporous materials can be highly effective at trace gas separations when they offer a high density of selective binding sites. Herein, we report that **sql-NbOFFIVE-bpe-Cu**, a new variant of a previously reported ultramicroporous square lattice, **sql**, topology material, **sql-SIFSIX-bpe-Zn**, can exist in two polymorphs. These polymorphs, **sql-NbOFFIVE-bpe-Cu-AA** (AA) and **sql-NbOFFIVE-bpe-Cu-AB** (AB), exhibit AAAA and ABAB packing of the **sql** layers, respectively. Whereas **NbOFFIVE-bpe-Cu-AA** (AA) is isostructural with **sql-SIFSIX-bpe-Zn**, each exhibiting intrinsic 1D channels, **sql-NbOFFIVE-bpe-Cu-AB** (AB) has two types of channels, the intrinsic channels and extrinsic channels between the **sql** networks. Gas and temperature induced transformations of the two polymorphs of **sql-NbOFFIVE-bpe-Cu** were investigated by pure gas sorption, single-crystal X-ray diffraction (SCXRD), variable temperature powder X-ray diffraction (VT-PXRD), and synchrotron PXRD. We observed that the extrinsic pore structure of **AB** resulted in properties with potential for selective C₃H₄/C₃H₆ separation. Subsequent dynamic gas breakthrough measurements revealed exceptional experimental C₃H₄/C₃H₆ selectivity (270) and a new benchmark for productivity (118 mmol g⁻¹) of polymer grade C₃H₆ (purity >99.99%) from a 1:99 C₃H₄/C₃H₆ mixture. Structural analysis, gas sorption studies, and gas adsorption kinetics enabled us to determine that a binding “sweet spot” for C₃H₄ in the extrinsic pores is behind the benchmark separation performance. Density-functional theory (DFT) calculations and Canonical Monte Carlo (CMC) simulations provided further insight into the binding sites of C₃H₄ and C₃H₆ molecules within these two hybrid ultramicroporous materials, HUMs. These results highlight, to our knowledge for the first time, how pore engineering through the study of packing polymorphism in layered materials can dramatically change the separation performance of a physisorbent.



INTRODUCTION

Metal–organic materials (MOMs)¹ such as metal–organic frameworks (MOFs)^{2–4} and porous coordination polymers (PCPs)⁵ are of topical interest because of their potential utility in, for example, gas storage, catalysis, biochemical imaging, and drug delivery.^{6–9} With respect to design, the diversity of their structures and compositions makes MOMs amenable to crystal engineering,¹⁰ which can enable systematic tuning of composition to control pore size, shape, and chemistry, *i.e.* “pore engineering”.^{11–15} Established approaches to pore engineering include interpenetration, flexibility, open metal sites (OMSs), functionalized ligands, counterion substitution, and pore space partition, which tend to lower pore volume.^{15–17} To our knowledge, pore engineering by different packing of adjacent layers, *i.e.* polymorphism, has not yet been reported.

Hybrid ultramicroporous materials (HUMs), a subclass of MOMs, are based on inorganic pillars such as MFSIX (e.g., GeF₆²⁻, TiF₆²⁻, SiF₆²⁻, SnF₆²⁻), FOXY (e.g., NbOF₅²⁻), and M'FFIVE (e.g., AlF₅²⁻, FeF₅²⁻). HUMs are of topical interest thanks to their strong and selective binding interactions with

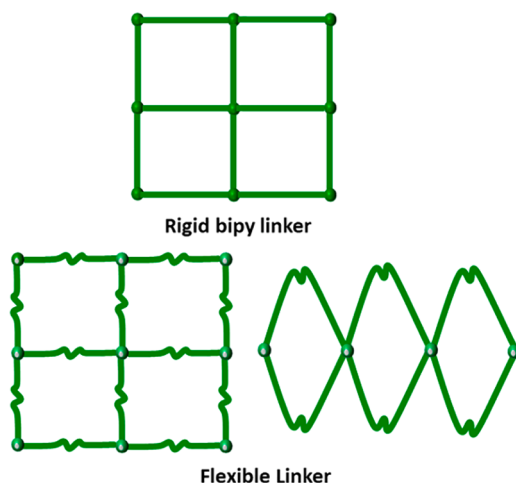
small gas molecules including CO₂ and hydrocarbons (HCs).^{18–26,11,20,27–37} Most HUMs are based on rigid organic linkers (e.g., pyrazine, 4,4'-bipyridine) and pillared by inorganic anions to afford three-dimensional rigid networks. Whether interpenetration of the networks occurs depends mainly on the length and rigidity of linker ligands (Table S2).^{18,19,21–23,38–40} Flexible linker ligands, e.g., 4,4'-dipyridylsulfide (dps), 4,4'-dipyridylsulfone, 4,4'-dipyridylsulfoxide, 1,2-bis(4-pyridyl)ethane (bpe), and 1,3-bis(4-pyridyl)propane (bpp), have the potential to form spiro-linked 1D coordination polymers that, when pillared by inorganic anions, afford 2D square lattice (**sql**) coordination networks (Scheme 1 and Table S3).^{24,27,41–44} **sql-SIFSIX-bpe-Zn**, SIFSIX = SiF₆²⁻, exemplifies such structures

Received: April 4, 2023

Published: May 19, 2023



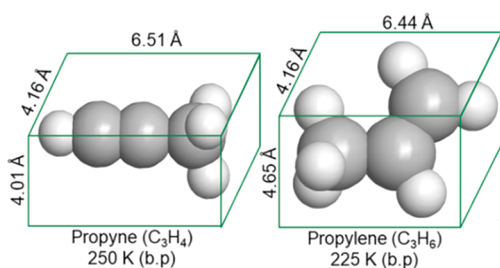
Scheme 1. Rigid Linker Ligands Tend to Generate sql Topology Coordination Networks (Above) Whereas Flexible Linkers Can Afford Either sql Networks or Spiro-Linked 1D Coordination Polymers (Below)



and was reported to exhibit high binding affinity for C_2H_2 via an induced fit mechanism enabled by flexibility.²⁷

Herein, we report that solvent-mediated crystallization can result in packing polymorphs of the related material **sql-NbOFFIVE-bpe-Cu**, **sql-NbOFFIVE-bpe-Cu-AA**, **AA**, and **sql-NbOFFIVE-bpe-Cu-AB**, **AB**, which exhibit AAAA and ABAB packing of their **sql** layers, respectively, and study the effect of crystal packing upon the C3 sorption properties of **sql-NbOFFIVE-bpe-Cu**. C3 sorption is relevant because propylene (C_3H_6) is a feedstock for the production of commodity chemicals such as acrylonitrile, propylene oxide, and polypropylene.^{45–47} Worldwide propylene production capacity was as high as 140 million tons in 2020, second only to that of ethylene among chemical building blocks.¹³ Further purification of C_3H_6 is needed because trace amounts ($\sim 1\%$) of propyne (C_3H_4) must be removed to afford polymer-grade ($\geq 99.95\%$) C_3H_6 for downstream applications.^{38,48} That C_3H_4 and C_3H_6 exhibit similar physicochemical properties (Scheme 2 and Table

Scheme 2. Comparison of the Molecular Structures and Physical Properties of C_3H_4 and C_3H_6



S1)⁴⁹ makes it a challenge for porous materials to produce polymer-grade C_3H_6 . The C3 sorption properties of **AA** and **AB** are addressed through a series of experimental and computational studies.

EXPERIMENTAL SECTION

All reagents and solvents were purchased commercially and used as received without further purification, except the precursor $CuNbOF_5 \cdot 4H_2O$, which was prepared by adapting a reported procedure.⁵⁰

Synthesis of **pcu-NbOFFIVE-bpe-Cu ($[Cu(NbOF_5)(bpe)_2]_n$).** In a typical reaction, **bpe** (6.3 mg, 0.035 mmol) in 2 mL of methanol was carefully layered onto $CuNbOF_5 \cdot 4H_2O$ (7 mg, 0.026 mmol) in 2 mL of water. Blue block crystals were obtained after 4 days in quantitative yield, collected by filtration and washed with methanol three times.

Synthesis of **sql-NbOFFIVE-bpe-Cu-AA- α , **AA- α** , ($[Cu(NbOF_5)(bpe)_2]_n$).** In a typical reaction, $CuNbOF_5 \cdot 4H_2O$ (0.0345 g, 0.13 mmol) and **bpe** (0.0276 g, 0.15 mmol) were added to 11.0 mL of H_2O/CH_3OH ($v/v = 9:2$). The solution was then sealed in a 14.5 mL vial and settled for 1 h. A light blue powder was obtained. This reaction can be readily scaled. When the reaction was conducted at room temperature or $60^\circ C$ for 2 months, blue block crystals of **AA- α** were obtained which were suitable for single-crystal X-ray diffraction (SCXRD) testing.

Preparation of **sql-NbOFFIVE-bpe-Cu-AA- β , **AA- β** .** A single crystal of the methanol exchanged phase of **AA- α** was activated at 333 K *in situ* on the goniometer of an SCXRD instrument. After 10 min SCXRD data showed that **AA- α** had transformed to **AA- β** . Bulk samples were prepared through activation at 333 K under vacuum.

Synthesis of **sql-NbOFFIVE-bpe-Cu-AB- α , **AB- α** , ($[Cu(NbOF_5)(bpe)_2]_n$).** In a typical reaction, a solution of $CuNbOF_5 \cdot 4H_2O$ (7 mg, 0.026 mmol) in 1 mL of water was carefully layered onto **bpe** (6.3 mg, 0.035 mmol) in 4 mL of 1,2-dichlorobenzene. Block shaped dark blue single crystals of **AB- α** were obtained after 3 days. The crystals were collected by filtration and washed with methanol three times, yield 85%.

Preparation of **sql-NbOFFIVE-bpe-Cu-AB- β_1 , **AB- β_1** .** Methanol exchanged **AB- α** was activated by heating at 333 K under vacuum for 12 h and then exposed to air or soaked in water to yield **AB- β_1** .

RESULTS AND DISCUSSION

Solvent diffusion of $CuNbOF_5 \cdot 4H_2O$ and **bpe** in various organic solvents and water at room temperature afforded single crystals of three polymorphs of $[Cu(NbOF_5)(bpe)_2]_n$: a 3D **pcu** network; two 2D **sql** networks. When using 1:1 H_2O/CH_3OH (v/v), single crystals of the 3D **pcu** network, **pcu-NbOFFIVE-bpe-Cu**, were obtained with bulk purity (Figures 1 and S12).

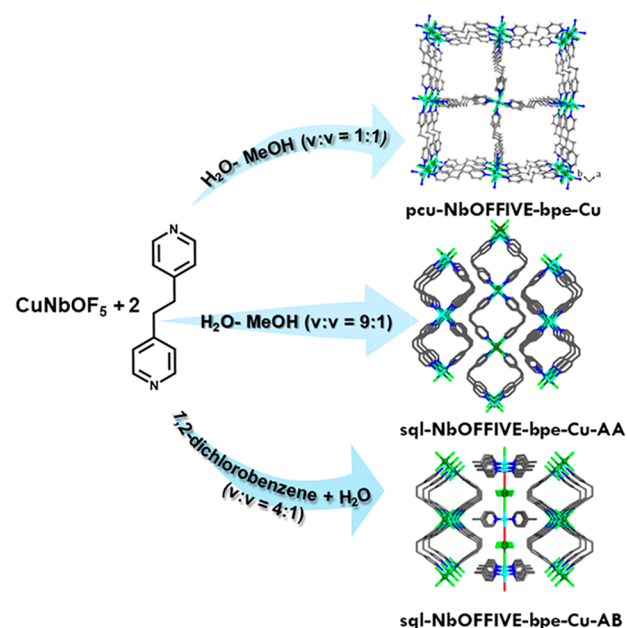


Figure 1. Synthetic conditions used and crystal structures of **pcu-NbOFFIVE-bpe-Cu**, **sql-NbOFFIVE-bpe-Cu-AA- α** , and **sql-NbOFFIVE-bpe-Cu-AB- α** . Color code: turquoise, Cu; green, Nb; red, O; bright green, F; blue, N; gray, C. Hydrogen atoms are omitted for clarity.

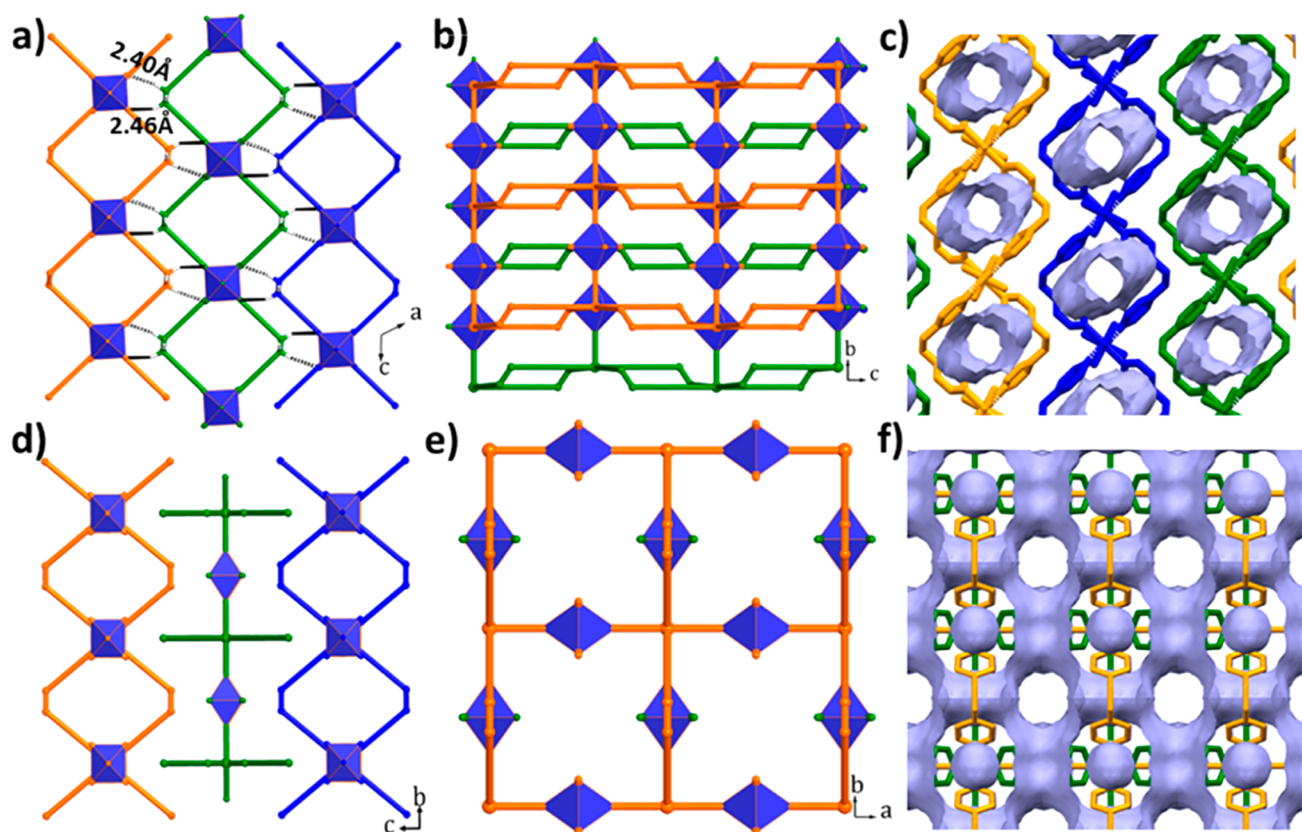


Figure 2. Comparisons of **sql-NbOFFIVE-bpe-Cu-AA- α** (a, b, c) and **sql-NbOFFIVE-bpe-Cu-AB- α** (d, e, f). Simplified crystal structure of **sql-NbOFFIVE-bpe-Cu-AA- α** along the *b* (a) and *a* axes (b); (c) 1D channels in **sql-NbOFFIVE-bpe-Cu-AA- α** ; Simplified crystal structures of **sql-NbOFFIVE-bpe-Cu-AB- α** along the *a* (d) and *c* axes (e); (f) 3D channels in **sql-NbOFFIVE-bpe-Cu-AB- α** . Color code: blue = NbOF₅; black = hydrogen bonds; Adjacent layers colored orange, green, and blue. Hydrogen atoms omitted for clarity.

SCXRD revealed that **pcu-NbOFFIVE-bpe-Cu** had crystallized in the tetragonal space group *P4/n* (Table S4). The non-interpenetrated network exhibits $\sim 9 \times 9$ Å pores, but crystals of **pcu-NbOFFIVE-bpe-Cu** did not survive guest removal, making it a first generation porous coordination polymer as classified by Kitagawa and co-workers (Figure S3).⁵ When the ratio of H₂O/CH₃OH was changed to 9:2 (v/v), single crystals of a 2D **sql** network variant, **AA- α** , were isolated (Figures 1, S1 and S5 upper). SCXRD analysis revealed that **AA- α** had crystallized in the monoclinic space group *C2/c* (Table S4). A 4:1 ratio of 1,2-dichlorobenzene and water (v/v) afforded single crystals of a polymorph of the same **sql** network, **AB- α** (Figures 1, S2, and S5 lower). SCXRD analysis revealed that **AB- α** had crystallized in tetragonal space group *P4₂/mmc* (Table S5). Bulk purities of **AA- α** and **AB- α** were confirmed by powder X-ray diffraction (PXRD, Figure S13).

Each Cu²⁺ cation in **AA- α** and **AB- α** is six-coordinate, coordinated by four N atoms from bpe ligands as well as one O atom and one F atom from two NbOF₅²⁻ anions (Figure S4). The pyridyl moieties are oriented in a *gauche* conformation about the C–C single bond backbone, resulting in a V-shaped bis(monodentate) linking mode. The layers in **AB- α** and **AA- α** stack differently. **AA- α** formed an AAAA layer arrangement similar to other **sql** topology HUMs (Figures 2, S5, and S6, some presented using simplified structures).^{11,24,27,41–44,51} Adjacent layers form H-bonds C(bpe ligand)–H...F(NbOF₅) of 2.40 and 2.46 Å that result in an arrangement reminiscent of a zipper. With respect to **AB- α** , NbOF₅²⁻ anion pillared Cu(bpe)₂ chains along the *a*-axis and *b*-axis lie in the *ab*-plane (Figures S5 and

S7). **AB- α** was found to exhibit ABAB stacking of layers, resulting in a pore structure distinct from that of **AA- α** and related materials.²⁷ The resulting ultramicroporous channels (3.96×5.56 Å², after subtracting the van der Waals radii, Figure 2f) represent 29.9% of the unit cell volume as calculated by PLATON.⁵² The 1D channels in **AA- α** resulted in a solvent-accessible space of 24.7% of the unit cell volume (Figure 2c). We anticipated that the inherent flexibility of bpe might enable induced fit or preferential binding toward C₃H₄ over C₃H₆¹⁰ and that the electronegative NbOF₅²⁻ anions lining the channels might preferentially bind alkynes vs alkenes (Figure 2c and 2f).^{24,42,53–56} We therefore undertook a study of the separation performance of these polymorphs toward C₃H₄ and C₃H₆.

As-synthesized **AB- α** transformed to a narrower-pore phase, **AB- β** , after methanol exchange at 333 K under vacuum for 12 h. We were unable to directly determine the crystal structure of activated (anhydrate) **AB- β** , as it captured water from air at low relative humidity (RH), as revealed by dynamic vapor sorption (DVS) (Figure S26). Figures S27 and S28 reveal that water vapor was adsorbed within minutes at 30% RH, 298 K. The SCXRD structure determined in air, **AB- β ₁**, was found to be a hydrate with twisted pores, twisted NbOF₅²⁻ anions, and undulating pillars, unlike **AB- α** (Figure S9). TGA data collected after holding at 80 °C for 2 h revealed no weight loss, further indicating that **AB- β** is fully activated and that water vapor was captured from the laboratory atmosphere (Figure S18). **AB- β ₁** crystallized in the tetragonal space group *P4₂/mnm* (Table S5). The distance between F atoms (*d*_{F...F}) in adjacent pillars changed from 6.33 Å in **AB- α** to 6.91 and 5.37 Å in **AB- β ₁** (Figure S10).

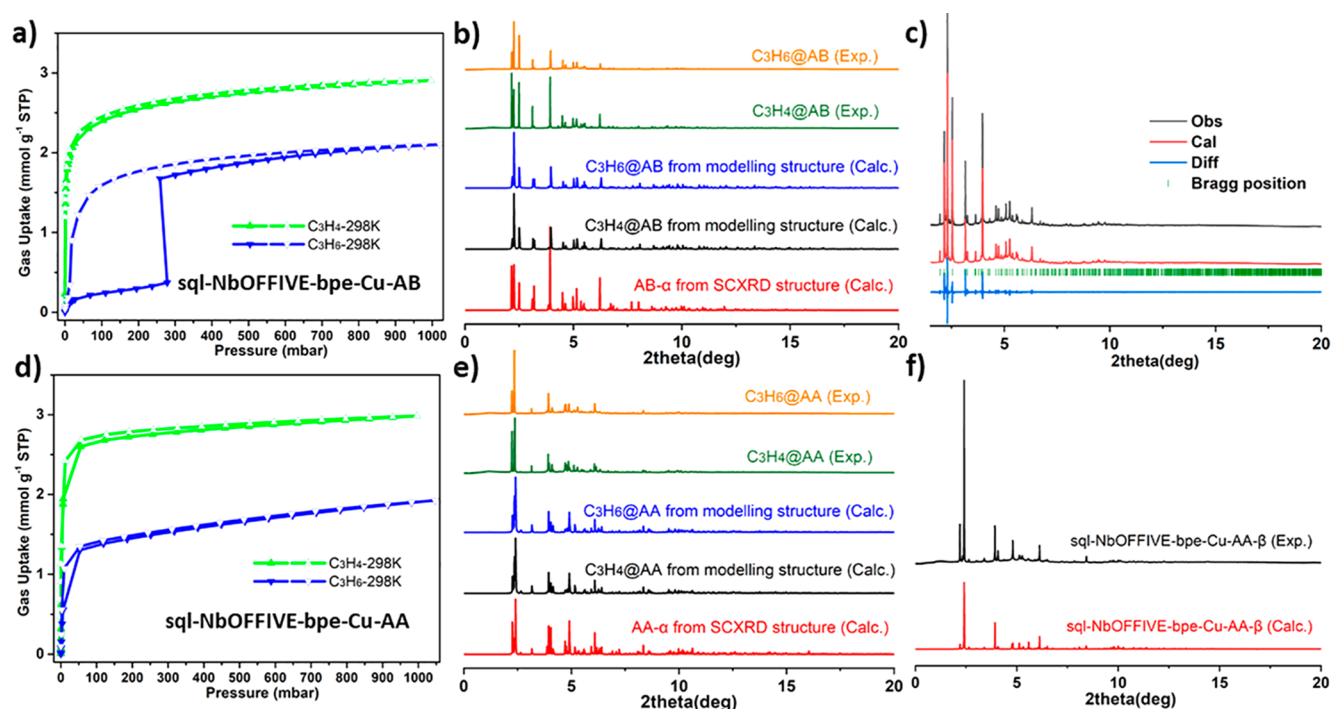


Figure 3. (a) C₃H₄ and C₃H₆ adsorption isotherms of **sql-NbOFFIVE-bpe-Cu-AB** collected at 298 K; (b) S-PXRD ($\lambda = 0.35424308$ Å) patterns of C₃H₄-loaded and C₃H₆-loaded **sql-NbOFFIVE-bpe-Cu-AB-α** compared with the PXRD patterns calculated from SCXRD and modeling data; (c) Pawley profile fit for **sql-NbOFFIVE-bpe-Cu-AB-β**. The experimental S-PXRD data are presented in black, calculated in red, and the difference between experimental and calculated in blue. Bragg reflections are shown as green bars. Crystal system = Tetragonal, Space group = $P4_2/mmm$, $a = b = 12.4888(4)$ Å, $c = 18.8761(6)$ Å, $V = 2944.1(2)$ Å³, $r_{wp} = 3.216\%$, $r_{exp} = 1.821\%$, $r_p = 3.127\%$, $GOF = 1.766$; (d) C₃H₄ and C₃H₆ adsorption isotherms of **sql-NbOFFIVE-bpe-Cu-AA** at 298 K; (e) S-PXRD ($\lambda = 0.35424308$ Å) patterns of C₃H₄-loaded and C₃H₆-loaded **sql-NbOFFIVE-bpe-Cu-AA-α** compared with their corresponding PXRD patterns calculated from SCXRD and modeling data; (f) S-PXRD patterns of experimental **sql-NbOFFIVE-bpe-Cu-AA-β** compared with calculated PXRD of **sql-NbOFFIVE-bpe-Cu-AA-β** from SCXRD.

Activation of **AA-α** resulted in **AA-β**. Heating at 333 K *in situ* under the SCXRD goniometer enabled structural determination of **AA-β** (Figure S8), which had crystallized in the monoclinic space group $I2/m$ (Table S4). The d_{hkl} value decreased from 7.1104 Å in **AA-α** to 6.9260 Å in **AA-β** (Figure S11).

These transformations were also investigated by variable-temperature PXRD (VT-PXRD). **AA-α** converted to **AA-β** by heating at 333 K under N₂, the PXRD pattern matching that calculated from the SCXRD structure (Figure S16a). Methanol exchanged **AB-α** transformed to desolvated **AB-β** after heating at 393 K under N₂ (Figure S16b). Methanol exchanged **AB-α** can also transform to **AB-β** by heating at 333 K under vacuum for 6 h (Figure S16c). The partially loaded **AB-β₁** phase was also observed by VT-PXRD at 333 K, its PXRD diffractogram matching the calculated PXRD pattern of **AB-β₁**. **AB-β** was observed to transform to **AA-β** after heating at 473 K under N₂ (Figure S16b).

To investigate the porosity of **AA** and **AB**, gas sorption isotherms of CO₂, at 195 K, and N₂, at 77 K, were collected (Figure S19). Prior to collection of sorption data, methanol exchanged **AA** and **AB** were activated at 333 K for 12 h under vacuum to generate their respective **β** forms. CO₂ adsorption by **AB** revealed a stepped isotherm profile with an inflection at low pressure (ca. 0.024 bar) and an uptake of ca. 1.5 mmol g⁻¹ after the first step.⁵⁷ A saturated CO₂ uptake of ~2.9 mmol g⁻¹ corresponds to almost 4 CO₂ molecules per unit cell. In the case of N₂ adsorption, an uptake of ~2.0 mmol g⁻¹ was observed. The corresponding values for **AA** revealed CO₂ and N₂ uptakes of ~3.5 mmol g⁻¹ and ~1.0 mmol g⁻¹, respectively. Langmuir surface areas of 356 m² g⁻¹ for **AA** and 295 m² g⁻¹ for **AB** were

calculated from 195 K CO₂ isotherms. The maximum pore size distributions derived from 195 K CO₂ data were determined to be 3.55 for **AA** and 6.04 Å for **AB**, matching the pore sizes derived from SCXRD data (Figure S19). For a larger probe size, such as N₂ at 77 K (3.6 Å for N₂ vs 3.3 Å for CO₂), **AA** shows lower uptake than that of **AB** because of its narrower pore.

Next, we studied the C₃H₄ and C₃H₆ adsorption properties of **AB** and **AA** at 273 and 298 K (Figures 3a, 3d, S20, and S21). The C₃H₄ sorption isotherm of **AB** revealed steep uptake at low pressure and an uptake of 3.04 mmol g⁻¹ at 1 bar and 298 K, significantly higher than its C₃H₆ uptake (2.10 mmol g⁻¹) under the same conditions. We note that the uptake of C₃H₆ was negligible at low pressure (0.01 mmol g⁻¹ at 0.001 bar; 0.1 mmol g⁻¹ at 0.01 bar; 0.23 mmol g⁻¹ at 0.1 bar), reflecting the stepped sorption isotherm.⁵⁷ The corresponding C₃H₄ uptakes were higher (1.20 mmol g⁻¹ at 0.001 bar; 1.93 mmol g⁻¹ at 0.01 bar; 2.40 mmol g⁻¹ at 0.1 bar, Figure S21). Similar stepped isotherms were reported for GEFSEX-dps-Cu, ELM-12, and ZU-13.^{11,58,59} The uptake ratio of C₃H₄/C₃H₆ for **AB** at 1 mbar is higher than that of NKMOF-11.¹² Sample regeneration was realized by exposure to vacuum at 333 K for as little as 10 min. Multiple sorption tests were performed, and similar sorption isotherms were observed, indicating good recyclability (Figure S22).

The differences between the single-component isotherms of C₃H₄ and C₃H₆ are indicative of potential utility for separation of C₃H₄/C₃H₆ binary mixtures. In the case of **AA**, the uptake ratio of C₃H₄/C₃H₆ at 1 mbar (~3.8) is much lower than that of **AB** (~120), although **AA** shows a similar uptake of C₃H₄ at 1 bar and lower uptake of C₃H₆ than **AB** (Figure S21). These results

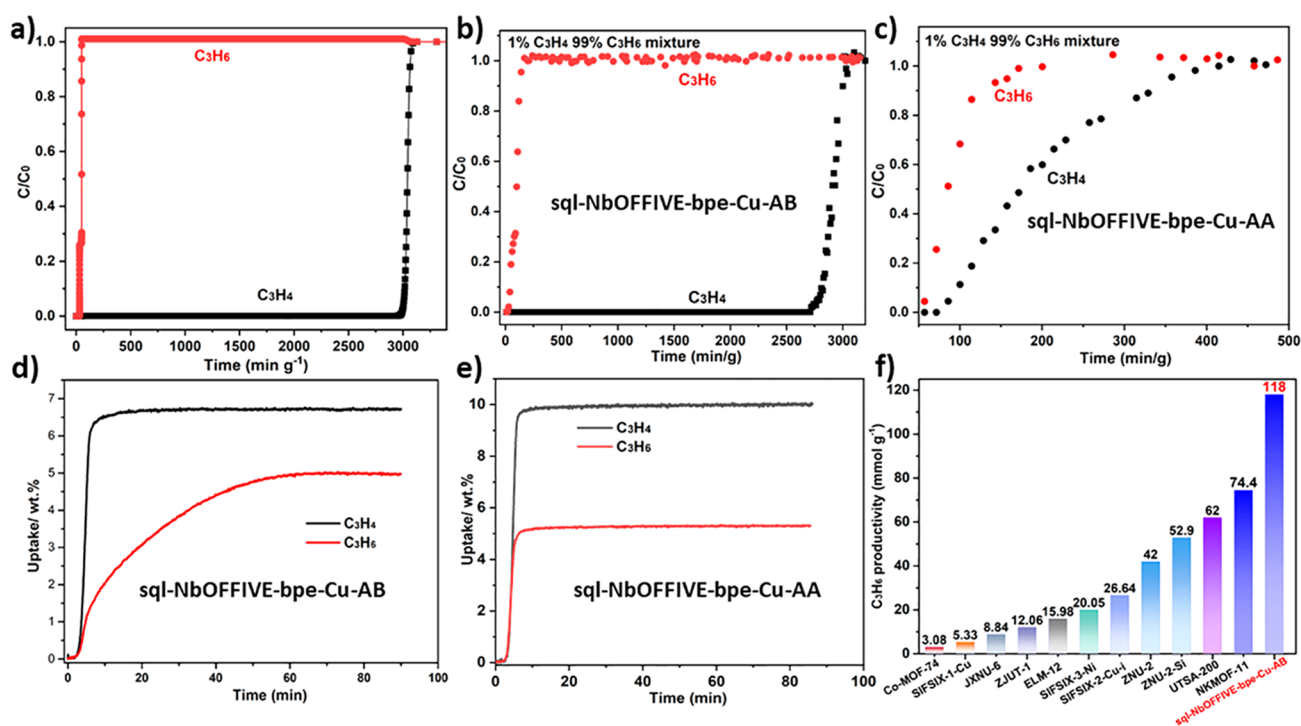


Figure 4. (a) Simulated breakthrough curves of $\text{sql-NbOFFIVE-bpe-Cu-AB}$ for separation of $\text{C}_3\text{H}_4/\text{C}_3\text{H}_6$ (1/99) mixture at 298 K; (b) Experimental breakthrough separation of $\text{sql-NbOFFIVE-bpe-Cu-AB}$ for $\text{C}_3\text{H}_4/\text{C}_3\text{H}_6$ (1/99) at 298 K (gas velocity: $1.0 \text{ cm}^3 \text{ min}^{-1}$); (c) Experimental breakthrough separation of $\text{sql-NbOFFIVE-bpe-Cu-AA}$ for $\text{C}_3\text{H}_4/\text{C}_3\text{H}_6$ (1/99) at 298 K (gas velocity: $1.0 \text{ cm}^3 \text{ min}^{-1}$); (d) Gravimetric kinetics of $\text{sql-NbOFFIVE-bpe-Cu-AB}$ for C_3H_4 and C_3H_6 uptake (0–1.0 bar) at 303 K; (e) Gravimetric kinetics of $\text{sql-NbOFFIVE-bpe-Cu-AA}$ for C_3H_4 and C_3H_6 uptake (1.0 bar) at 303 K; (f) Comparison of C_3H_6 productivity in representative benchmark materials for separation of 1/99 $\text{C}_3\text{H}_4/\text{C}_3\text{H}_6$ mixture.

indicate that **AB** offers stronger potential for separation of $\text{C}_3\text{H}_4/\text{C}_3\text{H}_6$ than **AA**.

Synchrotron PXRD (S-PXRD) data were collected for activated as well as C_3H_4 and C_3H_6 -loaded samples to study the guest-induced structural change. As shown in Figure 3b and 3e, S-PXRD diffractograms of C_3H_4 and C_3H_6 -loaded **AA** and **AB** support the presence of the corresponding α phases. The S-PXRD pattern of activated **AA- β** obtained by heating at 333 K under vacuum is consistent with the calculated pattern (Figure 3f). Pawley fitting for **AB- β** revealed tetragonal space group $P4_2/mmm$ (Figure 3c) and a unit cell volume of **AB- β** ($2944.1(2) \text{ \AA}^3$) slightly smaller than that of **AB- β_1** ($2954.6(4) \text{ \AA}^3$). These results indicate that both C_3H_4 and C_3H_6 can induce phase changes from the narrow-pore phases (**AA- β** and **AB- β**) to the respective open phases (**AA- α** and **AB- α**).

To quantify the potential of **AB** for separation of the challenging $\text{C}_3\text{H}_4/\text{C}_3\text{H}_6$ binary mixtures, ideal adsorption solution theory (IAST) calculations were conducted using Dual-site Langmuir–Freundlich (DSLFF) and 3-site Langmuir–Freundlich isotherm shape models^{60–62} (Figures S23 and S24, Tables S6 and S7). The calculated adsorption selectivity values for 1:99 and 1:1 $\text{C}_3\text{H}_4/\text{C}_3\text{H}_6$ binary mixtures are up to 220 and over 180 at 298 K and 1 bar, respectively. Simulated breakthrough data using a methodology described previously predicts excellent separation performance for $\text{C}_3\text{H}_4/\text{C}_3\text{H}_6$ (Figure 4a).^{63–67}

In order to experimentally evaluate the $\text{C}_3\text{H}_4/\text{C}_3\text{H}_6$ separation performance of **AA** and **AB**, we conducted dynamic column breakthrough (DCB) experiments that mimic typical process conditions with an inlet gas mixture composition of 1:99 (v/v) $\text{C}_3\text{H}_4/\text{C}_3\text{H}_6$.^{12,22} This $\text{C}_3\text{H}_4/\text{C}_3\text{H}_6$ gas mixture with a flow

rate of $1.0 \text{ cm}^3 \text{ min}^{-1}$ was passed through a fixed bed column (8 mm diameter) packed with sorbent at 1 bar and 298 K. The fixed beds of methanol exchanged samples were first activated by heating at 353 K in a $20 \text{ cm}^3 \text{ min}^{-1}$ flow of Helium for about 6 h. DCB experiments were commenced after samples were cooled to room temperature. Gas chromatography (GC) was used to monitor eluted components quantitatively at short sampling intervals (Figure S29; see Supporting Information for the experimental setup). As expected (Figure 4b and 4c), **AB** was indeed found to be more effective for $\text{C}_3\text{H}_4/\text{C}_3\text{H}_6$ separation than **AA**. For **AB**, C_3H_6 breakthrough occurred at 10 min g^{-1} , well before C_3H_4 (2710 min g^{-1}). This represents a C_3H_4 uptake capacity (1.2 mmol g^{-1} , Table S8) comparable to that of the previous benchmark sorbent, NKMOF-1-Ni (1.21 mmol g^{-1}) and Ni@FAU (1.59 mmol g^{-1}).^{49,68} During the time lag of 2710 min g^{-1} before breakthrough, GC data showed that the concentration of C_3H_4 in the effluent gas stream was $<1 \text{ ppm}$ (Table S8). According to the DCB profile obtained from a 1/99 mixture, the polymer-grade C_3H_6 productivity ($>99.99\%$ purity) of **AB** sets a new benchmark value of 118 mmol g^{-1} , beyond that of previous benchmark materials (NKMOF-11, 74.4 mmol g^{-1} ; UTSA-200, 62.0 mmol g^{-1} ; ZNU-2-Si, 52.9 mmol g^{-1} ; ZNU-2, 42 mmol g^{-1} ; SIFSIX-3-Ni, $20.05 \text{ mmol g}^{-1}$ and SIFSIX-2-Cu-i, $26.64 \text{ mmol g}^{-1}$, Figure 4f).^{12,13,38,48,69} Separation selectivity (α_{AC}) was calculated to be 270, exceeding that of reported HUMs with **sql** topology GeFSIX-dps-Cu (82.1), GeFSIX-dps-Zn (65.6).¹¹ That **AB** outperformed previous benchmark materials in terms of C_3H_6 productivity demonstrates that HUMs can offer both high selectivity and high uptake for challenging gas separations.

We also studied the pure gas adsorption kinetics for C_3H_4 and C_3H_6 using methanol exchanged samples, whereby activated samples of **AA** and **AB** were exposed to a constant flow of $10 \text{ cm}^3 \text{ min}^{-1}$ C_3H_4 and C_3H_6 at 303 K and 1.0 bar. As presented in Figure 4d, the slope of the kinetic curve for **AB** is much steeper for C_3H_4 than that of C_3H_6 , indicating faster adsorption kinetics for C_3H_4 . The kinetic curves of C_3H_4 and C_3H_6 level off at 6.8 wt % (1.7 mmol g^{-1}) after ca. 10 min and 2.5 wt % (1.2 mmol g^{-1}) after ca. 60 min, respectively. Regeneration tests were performed by heating the samples at 353 K under N_2 flow for ca. 1 h (flow rate: $60 \text{ cm}^3 \text{ min}^{-1}$), and no changes in uptake were observed after successive cycles (Figure S25). With respect to **AA**, the slope of the kinetic curve is almost the same for C_3H_4 and C_3H_6 , indicating similar adsorption kinetics for C_3H_4 and C_3H_6 (Figures 4e and S25). That gas adsorption kinetics in **AB** favors C_3H_4 over C_3H_6 is desirable for efficient gas separation during dynamic DCB tests.

Hydrolytic stability of a sorbent is a prerequisite for utility, prompting us to soak crystals of **AB** in water and perform water vapor sorption experiments using DVS. The water sorption experiment revealed a type I isotherm with approximately 15 wt % uptake at about 90% RH, which is consistent with the weight loss observed in the TGA curve ($\sim 12 \text{ wt } \%$, Figures S17 and S26). Cycling tests were performed 10 times and revealed that the sample retained stability when exposed to humidity (Figure S28). Crystals soaked in water for 5 days retained crystallinity (Figure S14).

Insight into the distinct sorption properties of **AA** and **AB** was gained through DFT calculations, which revealed that **AA** and **AB** have similar lattice energies, the **AB** to **AA** transformation being predicted to be exothermic by $-13.2 \text{ kJ mol}^{-1}$ per $Cu_2Nb_2O_2F_{10}(\text{bpe})_4$ formula unit. DFT was also used to identify the most plausible binding sites and their adsorption enthalpies whereas Canonical Monte Carlo (CMC) simulations were conducted to obtain adsorbate occupancy or the density map comprising the binding site regions (see Supporting Information for further details on the computational methodology). For each framework, the energetically most plausible orientations for C_3H_4 and C_3H_6 are represented in Figure 5. The binding sites were identified using DFT calculations in which atomic positions were optimized so that the binding pockets can adapt to each adsorbate.

The resulting adsorption enthalpies C_3H_4 and C_3H_6 in **AA** were calculated to be -62.7 (C_3H_4) and -65.2 (C_3H_6) kJ mol^{-1} , respectively. These similar adsorption enthalpies and Gibbs free energy differences are indicative of poor selectivity for C3 hydrocarbons. These values are also in line with experimental data (Figure 4c). In contrast, the adsorption enthalpies of -69.0 (C_3H_4) and -53.0 (C_3H_6) kJ mol^{-1} calculated for **AB** suggest enhanced binding of C_3H_4 and weaker C_3H_6 binding compared to **AA**, also in line with experimental observations (Figure 4b). The 16 kJ mol^{-1} difference in adsorption enthalpy for **AB** is also found in the adsorption Gibbs free energy differences ΔG_{ads} of -24.4 (C_3H_4) and -8.5 (C_3H_6) kJ mol^{-1} , where a difference of only 4.4 kJ mol^{-1} was calculated for **AA**, with ΔG_{ads} values of -19.6 (C_3H_4) and -15.0 (C_3H_6) kJ mol^{-1} , respectively. For both adsorbates, there are hydrogen bonds between H atoms of the adsorbates and framework F atoms (Figure 5), as is typical for HUMs.^{70–73} A detailed analysis of these binding sites, including adsorption energy and distances, is summarized in Table S9. Binding site isosurfaces from CMC simulations are visualized in Tables S11 and S12 and reveal that the density fields, comprising adsorbate mass-middle point occupancies of

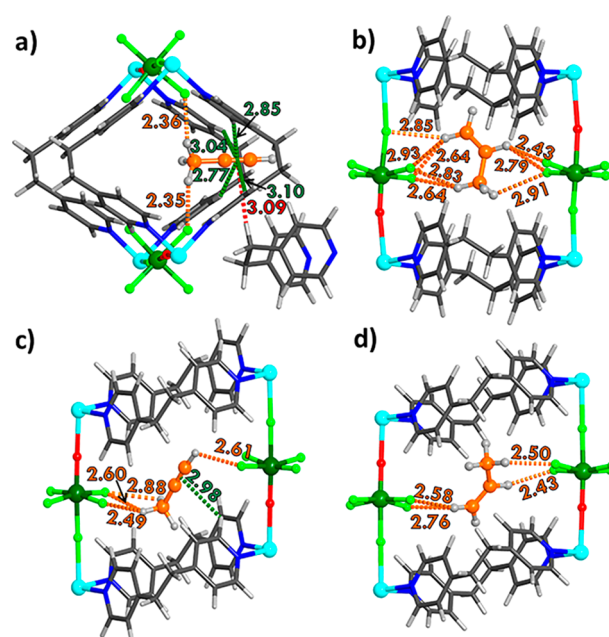


Figure 5. Binding sites of (a) C_3H_4 and (b) C_3H_6 in **sql-NbOFFIVE-bpe-Cu-AB** (a, b) and **sql-NbOFFIVE-bpe-Cu-AA** (c, d). The closest contacts (Å) between framework atoms and adsorbates are highlighted in orange for C–H...F, green for C–H... π , and red for C–H (with another framework)... π .

successful insertion moves, of C_3H_4 are larger than those of C_3H_6 for all frameworks. This can be attributed to the more linear geometry of C_3H_4 resulting in a larger binding area. Furthermore, the CMC results validate the preferred positions of the adsorbates in the framework and its channels in the vicinity of framework F atoms, which can be observed by merging the binding site outcomes from DFT and CMC (Figures S31 and S32). The four modeled crystal structures were used to calculate PXRD patterns, which are a good match for both the experimental S-PXRD data and the PXRD patterns calculated from SCXRD data (Figure 3b, 3e).

CONCLUSIONS

In summary, two packing polymorphs of an **sql** network with intrinsic ultramicropores, **AA** and **AB**, exhibit AAAA and ABAB packing of the **sql** layers, respectively. **AA** is isostructural with **sql-SIFSIX-bpe-Zn** and exhibits intrinsic 1D channels within each **sql** network. **AB** exhibits both intrinsic channels and extrinsic channels between the **sql** networks that arise from the different crystal packing of adjacent layers. Both polymorphs were found to display phase transformations induced by pressure and temperature. **AB** was found to be the most interesting sorbent in terms of sorption properties, as it exhibits excellent C_3H_4/C_3H_6 separation performance as indicated by a new high for C_3H_4/C_3H_6 experimental selectivity (270) and a new benchmark for polymer-grade C_3H_6 productivity (118 mmol g^{-1}) from a 1:99 C_3H_4/C_3H_6 binary mixture. Modeling studies provided insight into the selective binding sites for C_3H_4 . This work has not only resulted in a new benchmark for C_3H_4 separation from C_3H_6 but also brings a new approach to pore engineering. Specifically, whereas the packing polymorphs exhibit similar surface areas, their pore chemistry, size, and shape are distinctly different.

■ ASSOCIATED CONTENT

SI Supporting Information

The Supporting Information is available free of charge at <https://pubs.acs.org/doi/10.1021/jacs.3c03505>.

Experimental and characterization details; additional figures and images; PXRD patterns; VT-PXRD patterns; TGA analysis, DVS analysis, and Sorption isotherms. (PDF)

Accession Codes

CCDC 1973753 and 2154469–2154473 contain the supplementary crystallographic data for this paper. These data can be obtained free of charge via www.ccdc.cam.ac.uk/data_request/cif, or by emailing data_request@ccdc.cam.ac.uk, or by contacting The Cambridge Crystallographic Data Centre, 12 Union Road, Cambridge CB2 1EZ, UK; fax: +44 1223 336033.

■ AUTHOR INFORMATION

Corresponding Author

Michael J. Zaworotko – Bernal Institute, Department of Chemical Sciences, University of Limerick, Limerick V94 T9PX, Republic of Ireland; orcid.org/0000-0002-1360-540X; Email: xtal@ul.ie

Authors

Mei-Yan Gao – Bernal Institute, Department of Chemical Sciences, University of Limerick, Limerick V94 T9PX, Republic of Ireland; orcid.org/0000-0001-6628-5190

Andrey A. Bezrukov – Bernal Institute, Department of Chemical Sciences, University of Limerick, Limerick V94 T9PX, Republic of Ireland

Bai-Qiao Song – Bernal Institute, Department of Chemical Sciences, University of Limerick, Limerick V94 T9PX, Republic of Ireland

Meng He – Department of Chemistry, University of Manchester, Manchester M13 9PL, U.K.; orcid.org/0000-0001-7373-9779

Sousa Javan Nikkhah – Bernal Institute, Department of Chemical Sciences, University of Limerick, Limerick V94 T9PX, Republic of Ireland; orcid.org/0000-0003-1725-4069

Shi-Qiang Wang – Institute of Materials Research and Engineering (IMRE), Agency for Science, Technology and Research (A*STAR), 138634, Singapore; orcid.org/0000-0003-1213-8317

Naveen Kumar – Bernal Institute, Department of Chemical Sciences, University of Limerick, Limerick V94 T9PX, Republic of Ireland

Shaza Darwish – Bernal Institute, Department of Chemical Sciences, University of Limerick, Limerick V94 T9PX, Republic of Ireland; orcid.org/0000-0001-9397-6886

Debobroto Sensharma – Bernal Institute, Department of Chemical Sciences, University of Limerick, Limerick V94 T9PX, Republic of Ireland; orcid.org/0000-0002-4918-0730

Chenghua Deng – Bernal Institute, Department of Chemical Sciences, University of Limerick, Limerick V94 T9PX, Republic of Ireland

Jiangnan Li – Department of Chemistry, University of Manchester, Manchester M13 9PL, U.K.

Lunjie Liu – Department of Materials Science and Engineering, Southern University of Science and Technology, Shenzhen, Guangdong 518055, China

Rajamani Krishna – Van't Hoff Institute for Molecular Sciences, University of Amsterdam, 1098 XH, Amsterdam, Netherlands; orcid.org/0000-0002-4784-8530

Matthias Vandichel – Bernal Institute, Department of Chemical Sciences, University of Limerick, Limerick V94 T9PX, Republic of Ireland; orcid.org/0000-0003-1592-0726

Sihai Yang – Department of Chemistry, University of Manchester, Manchester M13 9PL, U.K.; orcid.org/0000-0002-1111-9272

Complete contact information is available at: <https://pubs.acs.org/10.1021/jacs.3c03505>

Notes

The authors declare no competing financial interest.

■ ACKNOWLEDGMENTS

M.J.Z. acknowledges the support of the Science Foundation Ireland (16/IA/4624), the Irish Research Council (IRCLA/2019/167), and the European Research Council (ADG 885695). S.J.N. and M.V. acknowledge the Irish Centre for High-End Computing (ICHEC) for the provision of computational facilities and support. S.J.N. is grateful for the support by Enterprise Ireland and the European Union's Horizon 2020 research and innovation programme under the Marie Skłodowska-Curie (grant agreement no. 847402, project ID: MF20210297). We are especially grateful to ESRF for access to beamline ID22 and the Diamond Light Source for access to beamline I19, as well as the beamline scientists for their support.

■ REFERENCES

- (1) Perry, J. J.; Perman, J. A.; Zaworotko, M. J. Design and synthesis of metal-organic frameworks using metal-organic polyhedra as supermolecular building blocks. *Chem. Soc. Rev.* **2009**, *38*, 1400–1417.
- (2) Li, J. R.; Sculley, J.; Zhou, H. C. Metal-organic frameworks for separations. *Chem. Rev.* **2012**, *112*, 869–932.
- (3) Yaghi, O. M.; O'Keeffe, M.; Ockwig, N. W.; Chae, H. K.; Eddaoudi, M.; Kim, J. Reticular synthesis and the design of new materials. *Nature* **2003**, *423*, 705–714.
- (4) Furukawa, H.; Cordova, K. E.; O'Keeffe, M.; Yaghi, O. M. The Chemistry and Applications of Metal-Organic Frameworks. *Science* **2013**, *341*, 1230444.
- (5) Kitagawa, S.; Kitaura, R.; Noro, S. Functional porous coordination polymers. *Angew. Chem., Int. Ed.* **2004**, *43*, 2334–2375.
- (6) Sui, J.; Liu, H.; Hu, S.; Sun, K.; Wan, G.; Zhou, H.; Zheng, X.; Jiang, H. L. A General Strategy to Immobilize Single-Atom Catalysts in Metal-Organic Frameworks for Enhanced Photocatalysis. *Adv. Mater.* **2022**, *34*, 2109203.
- (7) Moussa, Z.; Hmadeh, M.; Abiad, M. G.; Dib, O. H.; Patra, D. Encapsulation of curcumin in cyclodextrin-metal organic frameworks: Dissociation of loaded CD-MOFs enhances stability of curcumin. *Food Chem.* **2016**, *212*, 485–494.
- (8) Mortada, B.; Matar, T. A.; Sakaya, A.; Atallah, H.; Kara Ali, Z.; Karam, P.; Hmadeh, M. Postmetalated Zirconium Metal Organic Frameworks as a Highly Potent Bactericide. *Inorg. Chem.* **2017**, *56*, 4739–4745.
- (9) Das, M. C.; Xiang, S.; Zhang, Z.; Chen, B. Functional mixed metal-organic frameworks with metalloligands. *Angew. Chem., Int. Ed.* **2011**, *50*, 10510–10520.
- (10) Zhu, A. X.; Yang, Q. Y.; Mukherjee, S.; Kumar, A.; Deng, C. H.; Bezrukov, A. A.; Shivanna, M.; Zaworotko, M. J. Tuning the Gate-Opening Pressure in a Switching pcu Coordination Network, X-pcu-5-Zn, by Pillar-Ligand Substitution. *Angew. Chem., Int. Ed.* **2019**, *58*, 18212–18217.
- (11) Ke, T.; Wang, Q.; Shen, J.; Zhou, J.; Bao, Z.; Yang, Q.; Ren, Q. Molecular Sieving of C2 -C3 Alkene from Alkyne with Tuned

Threshold Pressure in Robust Layered Metal-Organic Frameworks. *Angew. Chem., Int. Ed.* **2020**, *59*, 12725–12730.

(12) Peng, Y. L.; Wang, T.; Jin, C.; Li, P.; Suepaul, S.; Beemer, G.; Chen, Y.; Krishna, R.; Cheng, P.; Pham, T.; Space, B.; Zaworotko, M. J.; Zhang, Z. A robust heterometallic ultramicroporous MOF with ultrahigh selectivity for propyne/propylene separation. *J. Mater. Chem. A* **2021**, *9*, 2850–2856.

(13) Jiang, Y.; Hu, J.; Wang, L.; Sun, W.; Xu, N.; Krishna, R.; Duttwyler, S.; Cui, X.; Xing, H.; Zhang, Y. Comprehensive Pore Tuning in an Ultrastable Fluorinated Anion Cross-Linked Cage-Like MOF for Simultaneous Benchmark Propyne Recovery and Propylene Purification. *Angew. Chem., Int. Ed.* **2022**, *61*, e202200947.

(14) Guo, L.; Savage, M.; Carter, J. H.; Han, X.; da Silva, I.; Manuel, P.; Rudic, S.; Tang, C. C.; Yang, S.; Schroder, M. Direct Visualization of Supramolecular Binding and Separation of Light Hydrocarbons in MFM-300(In). *Chem. Mater.* **2022**, *34*, 5698–5705.

(15) Lin, R. B.; Zhang, Z.; Chen, B. Achieving High Performance Metal-Organic Framework Materials through Pore Engineering. *Acc. Chem. Res.* **2021**, *54*, 3362–3376.

(16) Hong, A. N.; Yang, H.; Bu, X.; Feng, P. Pore space partition of metal-organic frameworks for gas storage and separation. *EnergyChem.* **2022**, *4*, 100080.

(17) Kokcam-Demir, U.; Goldman, A.; Esrafil, L.; Gharib, M.; Morsali, A.; Weingart, O.; Janiak, C. Coordinatively unsaturated metal sites (open metal sites) in metal-organic frameworks: design and applications. *Chem. Soc. Rev.* **2020**, *49*, 2751–2798.

(18) Subramanian, S.; Zaworotko, M. J. Porous Solids by Design: $[\text{Zn}(4,4'\text{-bpy})_2(\text{SiF}_6)]_n \cdot x\text{DMF}$, a Single Framework Octahedral Coordination Polymer with Large Square Channel. *Angew. Chem., Int. Ed.* **1995**, *34*, 2127–2128.

(19) Cadiau, A.; Belmabkhout, Y.; Adil, K.; Bhatt, P. M.; Pillai, R. S.; Shkurenko, A.; Martineau-Corcoss, C.; Maurin, G.; Eddaoudi, M. Hydrolytically stable fluorinated metal-organic frameworks for energy-efficient dehydration. *Science* **2017**, *356*, 731–735.

(20) Song, B. Q.; Yang, Q. Y.; Wang, S. Q.; Vandichel, M.; Kumar, A.; Crowley, C.; Kumar, N.; Deng, C. H.; GasconPerez, V.; Lusi, M.; Wu, H.; Zhou, W.; Zaworotko, M. J. Reversible Switching between Nonporous and Porous Phases of a New SIFSIX Coordination Network Induced by a Flexible Linker Ligand. *J. Am. Chem. Soc.* **2020**, *142*, 6896–6901.

(21) Nugent, P.; Belmabkhout, Y.; Burd, S. D.; Cairns, A. J.; Luebke, R.; Forrest, K.; Pham, T.; Ma, S.; Space, B.; Wojtas, L.; Eddaoudi, M.; Zaworotko, M. J. Porous materials with optimal adsorption thermodynamics and kinetics for CO₂ separation. *Nature* **2013**, *495*, 80–84.

(22) Chen, K. J.; Madden, D. G.; Mukherjee, S.; Pham, T.; Forrest, K. A.; Kumar, A.; Space, B.; Kong, J.; Zhang, Q. Y.; Zaworotko, M. J. Synergistic sorbent separation for one-step ethylene purification from a four-component mixture. *Science* **2019**, *366*, 241–246.

(23) Cui, X.; Chen, K.; Xing, H.; Yang, Q.; Krishna, R.; Bao, Z.; Wu, H.; Zhou, W.; Dong, X.; Han, Y.; Li, B.; Ren, Q.; Zaworotko, M. J.; Chen, B. Pore chemistry and size control in hybrid porous materials for acetylene capture from ethylene. *Science* **2016**, *353*, 141–144.

(24) Wang, J.; Zhang, Y.; Su, Y.; Liu, X.; Zhang, P.; Lin, R. B.; Chen, S.; Deng, Q.; Zeng, Z.; Deng, S.; Chen, B. Fine pore engineering in a series of isoreticular metal-organic frameworks for efficient C₂H₂/CO₂ separation. *Nat. Commun.* **2022**, *13*, 200.

(25) Sensharma, D.; O'Hearn, D. J.; Koochaki, A.; Bezrukov, A. A.; Kumar, N.; Wilson, B. H.; Vandichel, M.; Zaworotko, M. J. The First Sulfate-Pillared Hybrid Ultramicroporous Material, SOFOUR-1-Zn, and Its Acetylene Capture Properties. *Angew. Chem., Int. Ed.* **2022**, *61*, e202116145.

(26) Scott, H. S.; Shivanna, M.; Bajpai, A.; Chen, K.-J.; Madden, D. G.; Perry, J. J., IV; Zaworotko, M. J. Enhanced Stability toward Humidity in a Family of Hybrid Ultramicroporous Materials Incorporating Cr₂O₇²⁻ Pillars. *Cryst. Growth Des.* **2017**, *17*, 1933–1937.

(27) Shivanna, M.; Otake, K. I.; Song, B. Q.; van Wyk, L. M.; Yang, Q. Y.; Kumar, N.; Feldmann, W. K.; Pham, T.; Suepaul, S.; Space, B.; Barbour, L. J.; Kitagawa, S.; Zaworotko, M. Benchmark acetylene

binding affinity and separation through induced fit in a flexible hybrid ultramicroporous material. *Angew. Chem., Int. Ed.* **2021**, *60*, 20383–20390.

(28) Lin, R. B.; Xiang, S.; Xing, H.; Zhou, W.; Chen, B. Exploration of porous metal-organic frameworks for gas separation and purification. *Coord. Chem. Rev.* **2019**, *378*, 87–103.

(29) Zhao, X.; Wang, Y.; Li, D. S.; Bu, X.; Feng, P. Metal-Organic Frameworks for Separation. *Adv. Mater.* **2018**, *30*, 1705189.

(30) Barnett, B. R.; Gonzalez, M. I.; Long, J. R. Recent Progress Towards Light Hydrocarbon Separations Using Metal-Organic Frameworks. *Trends Chem.* **2019**, *1*, 159–171.

(31) Lan, T.; Li, L.; Chen, Y.; Wang, X.; Yang, J.; Li, J. Opportunities and critical factors of porous metal-organic frameworks for industrial light olefins separation. *Mater. Chem. Front.* **2020**, *4*, 1954–1984.

(32) Wang, H.; Liu, Y.; Li, J. Designer Metal-Organic Frameworks for Size-Exclusion-Based Hydrocarbon Separations: Progress and Challenges. *Adv. Mater.* **2020**, *32*, 2002603.

(33) Pei, J.; Shao, K.; Zhang, L.; Wen, H. M.; Li, B.; Qian, G. Current Status of Microporous Metal-Organic Frameworks for Hydrocarbon Separations. *Top. Curr. Chem.* **2019**, *377*, 33.

(34) Li, H.; Li, L.; Lin, R.-B.; Zhou, W.; Zhang, Z.; Xiang, S.; Chen, B. Porous metal-organic frameworks for gas storage and separation: Status and challenges. *EnergyChem.* **2019**, *1*, 100006.

(35) Lin, R. B.; Xiang, S.; Zhou, W.; Chen, B. Microporous Metal-Organic Framework Materials for Gas Separation. *Chem.* **2020**, *6*, 337.

(36) Wang, B.; Xie, L. H.; Wang, X.; Liu, X. M.; Li, J.; Li, J. R. Applications of metal-organic frameworks for green energy and environment: New advances in adsorptive gas separation, storage and removal. *Green Energy Environ.* **2018**, *3*, 191–228.

(37) Wang, S. Q.; Mukherjee, S.; Zaworotko, M. J. Spiers Memorial Lecture: Coordination networks that switch between nonporous and porous structures: an emerging class of soft porous crystals. *Faraday Discuss.* **2021**, *231*, 9–50.

(38) Li, L.; Wen, H. M.; He, C.; Lin, R. B.; Krishna, R.; Wu, H.; Zhou, W.; Li, J.; Li, B.; Chen, B. A Metal-Organic Framework with Suitable Pore Size and Specific Functional Sites for the Removal of Trace Propyne from Propylene. *Angew. Chem., Int. Ed.* **2018**, *57*, 15183–15188.

(39) Shekhah, O.; Belmabkhout, Y.; Chen, Z.; Guillerme, V.; Cairns, A.; Adil, K.; Eddaoudi, M. Made-to-order metal-organic frameworks for trace carbon dioxide removal and air capture. *Nat. Commun.* **2014**, *5*, 4228.

(40) Shekhah, O.; Belmabkhout, Y.; Adil, K.; Bhatt, P. M.; Cairns, A. J.; Eddaoudi, M. A facile solvent-free synthesis route for the assembly of a highly CO₂ selective and H₂S tolerant NiSIFSIX metal-organic framework. *Chem. Commun.* **2015**, *51*, 13595–13598.

(41) Wang, J.; Zhang, Y.; Zhang, P.; Hu, J.; Lin, R. B.; Deng, Q.; Zeng, Z.; Xing, H.; Deng, S.; Chen, B. Optimizing Pore Space for Flexible-Robust Metal-Organic Framework to Boost Trace Acetylene Removal. *J. Am. Chem. Soc.* **2020**, *142*, 9744–9751.

(42) Shen, J.; He, X.; Ke, T.; Krishna, R.; van Baten, J. M.; Chen, R.; Bao, Z.; Xing, H.; Dinca, M.; Zhang, Z.; Yang, Q.; Ren, Q. Simultaneous interlayer and intralayer space control in two-dimensional metal-organic frameworks for acetylene/ethylene separation. *Nat. Commun.* **2020**, *11*, 6259.

(43) Lin, R. B.; Li, L. B.; Wu, H.; Arman, H.; Li, B.; Lin, R. G.; Zhou, W.; Chen, B. L. Optimized Separation of Acetylene from Carbon Dioxide and Ethylene in a Microporous Material. *J. Am. Chem. Soc.* **2017**, *139*, 8022–8028.

(44) Suen, M. C.; Chan, Z. K.; Chen, J. D.; Wang, J. C.; Hung, C. H. Syntheses and structures of three new coordination polymers generated from the flexible 1,3-bis(4-pyridyl)propane ligand and zinc salts. *Polyhedron* **2006**, *25*, 2325–2332.

(45) Cadiau, A.; Adil, K.; Bhatt, P. M.; Belmabkhout, Y.; Eddaoudi, M. A metal-organic framework-based splitter for separating propylene from propane. *Science* **2016**, *353*, 137–140.

(46) Zeng, H.; Xie, M.; Wang, T.; Wei, R.-J.; Xie, X.-J.; Zhao, Y.; Lu, W.; Li, D. Orthogonal-array dynamic molecular sieving of propylene/propane mixtures. *Nature* **2021**, *595*, 542–548.

- (47) Gao, M. Y.; Song, B. Q.; Sensharma, D.; Zaworotko, M. J. Crystal engineering of porous coordination networks for C3 hydrocarbon separation. *SmartMat* **2021**, *2*, 38–55.
- (48) Yang, L.; Cui, X.; Yang, Q.; Qian, S.; Wu, H.; Bao, Z.; Zhang, Z.; Ren, Q.; Zhou, W.; Chen, B.; Xing, H. A Single-Molecule Propyne Trap: Highly Efficient Removal of Propyne from Propylene with Anion-Pillared Ultramicroporous Materials. *Adv. Mater.* **2018**, *30*, 1705374.
- (49) Peng, Y. L.; He, C.; Pham, T.; Wang, T.; Li, P.; Krishna, R.; Forrest, K. A.; Hogan, A.; Suepaul, S.; Space, B.; Fang, M.; Chen, Y.; Zaworotko, M. J.; Li, J.; Li, L.; Zhang, Z.; Cheng, P.; Chen, B. Robust Microporous Metal-Organic Frameworks for Highly Efficient and Simultaneous Removal of Propyne and Propadiene from Propylene. *Angew. Chem., Int. Ed.* **2019**, *58*, 10209–10214.
- (50) Heier, K. R.; Poeppelmeier, K. R. Reinvestigation of CuNbOF₅·4H₂O. *J. Solid State Chem.* **1997**, *133*, 576–579.
- (51) Lin, M. J.; Jouaiti, A.; Pocić, D.; Kyritsakas, N.; Planeix, J. M.; Hosseini, M. W. Molecular tectonics: tubular crystals with controllable channel size and orientation. *Chem. Commun.* **2010**, *46*, 112–114.
- (52) Spek, A. L. Single-crystal structure validation with the program PLATON. *J. Appl. Crystallogr.* **2003**, *36*, 7–13.
- (53) Yang, L.; Cui, X.; Zhang, Z.; Yang, Q.; Bao, Z.; Ren, Q.; Xing, H. An Asymmetric Anion-Pillared Metal-Organic Framework as a Multisite Adsorbent Enables Simultaneous Removal of Propyne and Propadiene from Propylene. *Angew. Chem., Int. Ed.* **2018**, *57*, 13145–13149.
- (54) Li, J.; Bhatt, P. M.; Li, J.; Eddaoudi, M.; Liu, Y. Recent Progress on Microfine Design of Metal-Organic Frameworks: Structure Regulation and Gas Sorption and Separation. *Adv. Mater.* **2020**, *32*, 2002563.
- (55) Cui, W. G.; Hu, T. L.; Bu, X. H. Metal-Organic Framework Materials for the Separation and Purification of Light Hydrocarbons. *Adv. Mater.* **2020**, *32*, 1806445.
- (56) Qian, S.; Hu, J.; Wang, X.; Yang, L.; Suo, X.; Wang, Z.; Cui, X.; Xing, H. Anion-pillared microporous material incorporated mixed-matrix fiber adsorbents for removal of trace propyne from propylene. *AIChE J.* **2023**, e18091.
- (57) Yang, Q. Y.; Lama, P.; Sen, S.; Lusi, M.; Chen, K. J.; Gao, W. Y.; Shivanna, M.; Pham, T.; Hosono, N.; Kusaka, S.; Perry, J. J. t.; Ma, S.; Space, B.; Barbour, L. J.; Kitagawa, S.; Zaworotko, M. J. Reversible Switching between Highly Porous and Nonporous Phases of an Interpenetrated Diamondoid Coordination Network That Exhibits Gate-Opening at Methane Storage Pressures. *Angew. Chem., Int. Ed.* **2018**, *57*, 5684–5689.
- (58) Li, L.; Lin, R. B.; Krishna, R.; Wang, X.; Li, B.; Wu, H.; Li, J.; Zhou, W.; Chen, B. Flexible-Robust Metal-Organic Framework for Efficient Removal of Propyne from Propylene. *J. Am. Chem. Soc.* **2017**, *139*, 7733–7736.
- (59) Yang, L.; Cui, X.; Zhang, Y.; Yang, Q.; Xing, H. A highly sensitive flexible metal-organic framework sets a new benchmark for separating propyne from propylene. *J. Mater. Chem. A* **2018**, *6*, 24452–24458.
- (60) Gutierrez-Sevillano, J. J.; Calero, S.; Krishna, R. Separation of benzene from mixtures with water, methanol, ethanol, and acetone: highlighting hydrogen bonding and molecular clustering influences in CuBTC. *Phys. Chem. Chem. Phys.* **2015**, *17*, 20114–20124.
- (61) Gutiérrez-Sevillano, J. J.; Calero, S.; Krishna, R. Selective Adsorption of Water from Mixtures with 1-Alcohols by Exploitation of Molecular Packing Effects in CuBTC. *J. Phys. Chem. C* **2015**, *119*, 3658–3666.
- (62) Pan, H.; Ritter, J. A.; Balbuena, P. B. Examination of the Approximations Used in Determining the Isothermic Heat of Adsorption from the Clausius-Clapeyron Equation. *Langmuir* **1998**, *14*, 6323–6327.
- (63) Krishna, R. Metrics for Evaluation and Screening of Metal-Organic Frameworks for Applications in Mixture Separations. *ACS Omega* **2020**, *5*, 16987–17004.
- (64) Krishna, R. Methodologies for screening and selection of crystalline microporous materials in mixture separations. *Sep. Purif. Technol.* **2018**, *194*, 281–300.
- (65) Krishna, R. The Maxwell-Stefan description of mixture diffusion in nanoporous crystalline materials. *Microporous Mesoporous Mater.* **2014**, *185*, 30–50.
- (66) Krishna, R. Methodologies for evaluation of metal-organic frameworks in separation applications. *RSC Adv.* **2015**, *5*, 52269–52295.
- (67) Krishna, R. Screening metal-organic frameworks for mixture separations in fixed-bed adsorbents using a combined selectivity/capacity metric. *RSC Adv.* **2017**, *7*, 35724–35737.
- (68) Chai, Y.; Han, X.; Li, W.; Liu, S.; Yao, S.; Wang, C.; Shi, W.; da-Silva, I.; Manuel, P.; Cheng, Y.; Daemen, L. D.; Ramirez-Cuesta, A. J.; Tang, C. C.; Jiang, L.; Yang, S.; Guan, N.; Li, L. Control of zeolite pore interior for chemoselective alkyne/olefin separations. *Science* **2020**, *368*, 1002–1006.
- (69) Jiang, Y.; Wang, L.; Yan, T.; Hu, J.; Sun, W.; Krishna, R.; Wang, D.; Gu, Z.; Liu, D.; Cui, X.; Xing, H.; Zhang, Y. Insights into the thermodynamic-kinetic synergistic separation of propyne/propylene in anion pillared cage MOFs with entropy-enthalpy balanced adsorption sites. *Chem. Sci.* **2023**, *14*, 298–309.
- (70) Gao, M. Y.; Sensharma, D.; Bezrukov, A. A.; Andaloussi, Y. H.; Darwish, S.; Deng, C.; Vandichel, M.; Zhang, J.; Zaworotko, M. J. A Robust Molecular Porous Material for C₂H₂/CO₂ Separation. *Small* **2023**, *19*, e2206945.
- (71) Wang, J. X.; Liang, C.-C.; Gu, X.-W.; Wen, H.-M.; Jiang, C.; Li, B.; Qian, G.; Chen, B. Recent advances in microporous metal-organic frameworks as promising adsorbents for gas separation. *J. Mater. Chem. A* **2022**, *10*, 17878–17916.
- (72) Li, X.; Bian, H.; Huang, W.; Yan, B.; Wang, X.; Zhu, B. A review on anion-pillared metal-organic frameworks (APMOFs) and their composites with the balance of adsorption capacity and separation selectivity for efficient gas separation. *Coord. Chem. Rev.* **2022**, *470*, 214714.
- (73) Ebadi Amooghin, A.; Sanaeepour, H.; Luque, R.; Garcia, H.; Chen, B. Fluorinated metal-organic frameworks for gas separation. *Chem. Soc. Rev.* **2022**, *51*, 7427–7508.

Recommended by ACS

Fine-Tuning MOFs with Amino Group for One-Step Ethylene Purification from the C2 Hydrocarbon Mixture

Mingxing Zhang, Su Wang, *et al.*

MAY 18, 2023
INORGANIC CHEMISTRY

READ 

Modulating Charges of Dual Sites in Multivariate Metal-Organic Frameworks for Boosting Selective Aerobic Epoxidation of Alkenes

Hanlin Liu, Guodong Li, *et al.*

MAY 10, 2023
JOURNAL OF THE AMERICAN CHEMICAL SOCIETY

READ 

Flexing of a Metal-Organic Framework upon Hydrocarbon Adsorption: Atomic Level Insights from Neutron Scattering

Benjamin A. Trump, Shane G. Telfer, *et al.*

JANUARY 31, 2023
CHEMISTRY OF MATERIALS

READ 

Combination of Low-Polar and Polar Binding Sites in Aliphatic MOFs for the Efficient C₂H₆/C₂H₄ Separation

Jingyi Zhou, Qiwei Yang, *et al.*

JANUARY 06, 2023
ACS APPLIED MATERIALS & INTERFACES

READ 

Get More Suggestions >

Supplementary Information for

Highly Productive C₃H₄/C₃H₆ Trace Separation by a Packing Polymorph of a Layered Hybrid Ultramicroporous Material

Mei-Yan Gao,^a Andrey A. Bezrukov,^a Bai-Qiao Song,^a Meng He,^b Sousa Javan Nikkhah,^a Shi-Qiang Wang,^d Naveen Kumar,^a Shaza Darwish,^a Debobroto Sensharma,^a Chenghua Deng,^a Jiangnan Li,^b Lunjie Liu,^e Rajamani Krishna,^c Matthias Vandichel,^a Sihai Yang,^b and Michael J. Zaworotko^{a*}

[a] Bernal Institute, Department of Chemical Sciences, University of Limerick, Limerick V94 T9PX, Republic of Ireland
E-mail: xtal@ul.ie

[b] Department of Chemistry, University of Manchester, Manchester, M13 9PL, UK

[c] Van't Hoff Institute for Molecular Sciences, University of Amsterdam, Science Park 904, 1098 XH Amsterdam, Netherlands.

[d] Institute of Materials Research and Engineering (IMRE), Agency for Science, Technology and Research (A*STAR), 2 Fusionopolis Way 138634, Singapore

[e] Department of Materials Science and Engineering, Southern University of Science and Technology, Shenzhen, Guangdong, 518055, China.

Table of Contents

Characterization, Experimental Methods and Sorption Studies	3
Physical and Electronic Parameters of Sorbent	11
Summary of hybrid ultramicroporous materials (HUMs)	11
Tables of Crystal Data	13
Optical Image.....	15
Crystal Structures.....	15
PXRD Patterns	19
TGA Curves	21
Sorption Studies	22
Fitting Isotherms	24
IAST selectivity	25
Fitting Related Parameter	25
Experimental Breakthrough Related Data	26
Gravimetric Kinetics.....	27
Water Sorption	29
Experimental Setup of DCB	30
Modeling Studies	31
References.....	37

Characterization, Experimental Methods and Sorption Studies

1. Powder X-ray diffraction (PXRD)

Powder X-ray diffraction patterns were recorded on a PANalytical X'Pert MPD Pro (Cu K α , $\lambda = 1.5418 \text{ \AA}$) with a 1D X'Celerator strip detector. Experiments were conducted in continuous scanning mode with the goniometer in the theta-theta orientation. Incident beam optics included the Fixed Divergences slit with anti-scatter slit PreFIX module, with a $1/8^\circ$ divergence slit and a $1/4^\circ$ anti-scatter slit, as well as a 10 mm fixed incident beam mask and a Soller slit (0.04 rad). Divergent beam optics included a P7.5 anti-scatter slit, a Soller slit (0.04 rad), and a Ni β filter. The data were collected in the range of $2\theta = 3\text{-}50$. Raw data was then evaluated using the X'Pert HighScore Plus™ software V 4.1 (PANalytical, The Netherlands).

2. In-situ Variable Temperature Powder X-ray Diffraction (VT-PXRD)

Diffractograms at different temperatures were recorded using a PANalytical X'Pert Pro-MPD diffractometer equipped with a PIXcel3D detector operating in scanning line detector mode with an active length of 4 utilizing 255 channels. Anton Paar TTK 450 stage coupled with the Anton Paar TCU 110 Temperature Control Unit was used to record the variable temperature diffractograms. The diffractometer is outfitted with an Empyrean Cu LFF (long fine-focus) HR (9430 033 7300x) tube operated at 40 kV and 40 mA and Cu K α radiation ($\lambda_{\alpha} = 1.54056 \text{ \AA}$) was used for diffraction experiments. Continuous scanning mode with the goniometer in the theta-theta orientation was used to collect the data. Incident beam optics included the Fixed Divergences slit, with a $1/4^\circ$ divergence slit and a Soller slit (0.04 rad). Divergent beam optics included a P7.5 anti-scatter slit, a Soller slit (0.04 rad), and a Ni- β filter. In a typical experiment, 20 mg of sample was ground into a fine powder, and was loaded on a zero background sample holder made for Anton Paar TTK 450 chamber. The data was collected from $4^\circ\text{-}40^\circ$ (2θ) with a

step-size of 0.0167113° and a scan time of 50 seconds per step. Crude data were analyzed using the X'Pert HighScore Plus™ software V 4.1 (PANalytical, The Netherlands). The sample was heated up to 453 K under N_2 atmosphere.

3. Thermogravimetric analysis (TGA)

Thermograms were recorded under nitrogen using TGA instrument TA Q50 V20.13 Build 39. Aluminium pans and a flow rate of $60 \text{ cm}^3 \text{ min}^{-1}$ for the nitrogen gas were used for the experiments. The data was collected in the High Resolution Dynamic mode with a sensitivity of 1.0, a resolution of 4.0, and a temperature ramp of $10 \text{ }^\circ\text{C min}^{-1}$ up to $550 \text{ }^\circ\text{C}$. The data was evaluated using the T.A. Universal Analysis suite for Windows XP/Vista Version 4.5A.

4. Dynamic Vapor Sorption (DVS)

Dynamic water vapour sorption studies were performed on the sample using a dynamic vapour sorption system (Surface Measurement Systems, DVS Adventure) which gravimetrically measures the uptake and loss of vapour using air as a carrier gas. Pure water was used as the adsorbate for these measurements and temperature was maintained at 298 K by enclosing the system in a temperature-controlled incubator. Prior to measurement, the sample was in-situ activated at $100 \text{ }^\circ\text{C}$, 0 RH. The mass of the sample was determined by comparison to an empty reference pan and recorded by a high resolution microbalance with a precision of $0.1 \text{ }\mu\text{g}$. Sorption isotherm was measured from 0 to 95% RH step-wise with a convergence equilibrium criterion $dm/dt = 0.05 \text{ \%}/\text{min}$. The minimum and maximum equilibration times for each step were 10 and 360 min, respectively. The kinetics were measured between two points 0 and 30% RH with a convergence equilibrium criterion $dm/dt = 0.05 \text{ \%}/\text{min}$. The recyclability test was done by performing 10 cycles, each cycle consisting of 15 min adsorption step (90% RH) and 30 min desorption step (0% RH).

5. Gas sorption measurements.

For gas sorption experiments, gases were used as received from BOC Gases Ireland: He (99.999%), N₂ (99.9995%), CO₂ (99.995%), C₃H₄ (97.0%), C₃H₆ (99.5%). Before sorption measurements, activation of **sql-NbOFFIVE-bpe-Cu-AB** and **sql-NbOFFIVE-bpe-Cu-AA** were achieved by degassing the air-dried samples on a SmartVacPrep™ using dynamic vacuum and heating for 12 h (the sample heated from RT to 333 K with a ramp rate of 1°C min⁻¹). About 100 mg of activated samples were used for the measurements on Micromeritics Tristar II 3030 or Micromeritics 3Flex surface area and pore size analyzer 3500. A Julabo temperature controller was used to maintain a constant temperature in the bath throughout the experiment. The bath temperatures of 273 and 298 K were precisely controlled with a Julabo ME (v.2) recirculating control system containing a mixture of ethylene glycol and water. The low temperatures at 77 K and 195 K were controlled by a 4 L Dewar filled with liquid N₂ and dry ice/acetone, respectively. At every interval of two independent isotherms recorded for any sorbent, samples were regenerated by degassing over 30 min under high vacuum at 333 K, before commencing the next sorption experiment.

6. Breakthrough experiments.

In typical breakthrough experiments, MeOH exchanged **sql-NbOFFIVE-bpe-Cu-AB** (~0.5 g) or MeOH exchanged **sql-NbOFFIVE-bpe-Cu-AA** (~0.35 g) was placed in quartz tubing (8 mm diameter; 8 mm x 6 mm x 400 mm) to form fixed beds. First, the adsorbent bed was purged under a 20 cm³ min⁻¹ flow of He gas at 353 K for 6 hours prior to breakthrough experiment. Upon cooling to room temperature, the gas flow was switched to the desired C₃H₄/C₃H₆ gas mixture compositions (1:99), maintained at a total flow rate of 1.0 cm³ min⁻¹. Then, 1:99 C₃H₄/C₃H₆ binary breakthrough experiments were conducted at 298 K. The outlet composition

was continuously monitored by a Shimadzu Nexis GC-2030 gas chromatograph until complete breakthrough was achieved.

The C₃H₆ productivity (q) is defined by the breakthrough amount of C₃H₆, which is calculated by integration of the breakthrough curves f(t) during a period from τ_1 to τ_2 where the C₃H₆ purity is higher than or equal to a threshold value p:

$$q = \frac{C_i(\text{C}_3\text{H}_6)}{C_i(\text{C}_3\text{H}_6) + C_i(\text{C}_3\text{H}_4)} \times \left(\int_{\tau_1}^{\tau_2} f(t) dt \right)$$

7. Single Crystal X-ray diffraction

Single crystal X-ray diffraction data were collected on a Bruker Quest diffractometer equipped with a $I\mu\text{S}$ microfocus X-ray source Cu K α , ($\lambda = 1.54178 \text{ \AA}$); Mo K α , ($\lambda = 0.71073 \text{ \AA}$); Synchrotron ($\lambda = 0.4859 \text{ \AA}$), and CMOS detector. APEX3 or APEX4 was used for collecting, indexing, integrating and scaling the data.¹ An open-flow nitrogen attachment (Oxford Cryosystems) was used for low temperature measurements. Absorption corrections were performed by multi-scan method.² Space groups were determined using XPREP³ as implemented in APEX3. All the scaled data were solved using intrinsic phasing method (XT)⁴ and refined on F² using SHELXL⁵ inbuilt in OLEX2 v1.5 (2020) program.⁶ All non-hydrogen atoms present in the frameworks were refined anisotropically. Hydrogen atoms were located at idealized positions from the molecular geometry and refined isotropically with thermal parameters based on the equivalent displacement parameters of their carriers. Crystallographic data reported in this paper are summarized in Tables S4 and Table S5. These crystal structures have been deposited to the Cambridge Crystallographic Data Centre (CCDC 2154469-2154473, and 1973753).

8. Fitting of experimental data on pure component isotherms

The isotherm data for C₃H₄ in the flexible MOF at 298 K were fitted with the 2-site Langmuir-Freundlich model,⁸ where we distinguish two distinct adsorption sites A and B:

$$q = q_{A,sat} \frac{b_A p^{V_A}}{1 + b_A p^{V_A}} + q_{B,sat} \frac{b_B p^{V_B}}{1 + b_B p^{V_B}} \quad (1)$$

The isotherm data for C₃H₆ in the flexible MOF at 298 K were fitted with the 3-site Langmuir-Freundlich model,^{9, 10} where we distinguish three distinct adsorption sites A, B, and C:

$$q = q_{A,sat} \frac{b_A p^{V_A}}{1 + b_A p^{V_A}} + q_{B,sat} \frac{b_B p^{V_B}}{1 + b_B p^{V_B}} + q_{C,sat} \frac{b_C p^{V_C}}{1 + b_C p^{V_C}} \quad (2)$$

The unary isotherm fit parameters are provided in Tables S6 and S7.

9. Adsorption Selectivity Calculations.

The detailed methodology for calculating the amount of A and B adsorption from a mixture by ideal adsorbed solution theory (IAST) is described elsewhere.¹¹ The adsorption selectivity is finally defined as:

$$Selectivity = \frac{q_A / q_B}{p_A / p_B} \quad (3)$$

where q_i (i = A or B) is the uptake quantity in the mixture and p_i is the feeding partial pressure of component i.

10. Breakthrough simulations

The performance of industrial fixed bed adsorbers is dictated by a combination of adsorption selectivity and uptake capacity. Transient breakthrough simulations were carried out for 1/99 C₃H₄/C₃H₆ mixtures in the flexible MOF operating at a total pressure of 100 kPa, and temperatures of 298 K, using the methodology described in earlier publications.¹²⁻¹⁶ In these simulations the intra-crystalline diffusional influences are considered to be of negligible importance. The breakthrough simulations are plotted as follows. The y-axis is the

dimensionless concentrations of each component at the exit of the fixed bed, normalized with respect to the inlet feed concentrations, c / c_0 . The x -axis is

$$\frac{t}{m_{ads}} = \frac{(\text{time in min})}{(\text{g MOF packed in tube})} = \text{min g}^{-1}$$

11. Separation factor / Separation selectivity calculations.

The amount of adsorbed gas i (q_i) is calculated from the breakthrough curve as follows:

$$q_i = \frac{V_i T_0 - V_{dead} - \int_0^{t_0} V_e \Delta T}{m}$$

Here, V_i is the influent flow rate of gas ($\text{cm}^3 \text{min}^{-1}$), V_e is the effluent flow rate of gas ($\text{cm}^3 \text{min}^{-1}$), V_{dead} is the dead volume of the system (cm^3), T_0 is the adsorption time (min) and m is the mass of the sorbent (g).¹⁷

On approximation, this simplifies to:

$$q_i = \frac{V_T \Delta T P_i}{m}$$

V_T is the total flow rate of gas ($\text{cm}^3 \text{min}^{-1}$), P_i is the partial pressure of gas i (bar) and ΔT is the time for initial breakthrough of gas i to occur (min).¹⁸ The separation factor, also known as separation selectivity (α_{AC}) for the breakthrough experiment *i.e.* breakthrough derived selectivity is determined as follows:

$$\alpha = \frac{q_1 y_2}{q_2 y_1}$$

y_i is the partial pressure of gas i in the gas mixture. In the case where one gas component has negligible adsorption, the amount of gas adsorbed is treated as $\leq 1 \text{ cm}^3$ for calculations.

12. Modeling Studies

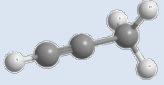
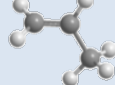
Periodic Density Functional Theory (DFT) calculations were performed using the projected augmented wave (PAW) formalism³³ as implemented in the Vienna Ab Initio Simulation Package (VASP 5.4.4),^{34, 35} on 1x2x1 and 2x2x1 supercells for **sql-NbOFFIVE-bpe-Cu-AA- α** , and **sql-NbOFFIVE-bpe-Cu-AB- α** , respectively, employing the BEEF-vdW exchange-correlation functional.³⁶ Subsequently, the adsorption of C₃H₄ and C₃H₆ was studied in both supercells, and plausible binding sites were optimized at the Γ -point (using the experimental cell parameters) with the conjugate gradient algorithm with force and electronic convergence criteria of 0.01 eV/Å and 10⁻⁶ eV, a Gaussian smearing of 0.02 eV, an energy cut-off of 550 eV, and assuming a ferromagnetic coupling between of the unpaired electrons on each Cu atom (one unpaired electron per Cu). A partial Hessian vibrational analysis was performed by numerically displacing the atomic coordinates of the investigated adsorbates in x, y, and z-directions with ± 0.01 Å to verify the binding sites as local minima on the potential energy surface. Furthermore, the adsorption enthalpies (at 298 K) and zero-point corrected adsorption energies and adsorption Gibbs free energies (at 298 K) were calculated with the post-processing toolkit TAMKIN.³⁷

Canonical Monte Carlo (CMC) simulations³⁸ were performed to confirm the main binding site locations for the adsorbates C₃H₄ and C₃H₆ in the frameworks. CMC simulations were performed using RASPA^{39, 40}, and Materials Studio⁴¹ at 298.15 K on 1x2x1 and 2x2x1 supercells of **sql-NbOFFIVE-bpe-Cu-AA- α** and **sql-NbOFFIVE-bpe-Cu-AB- α** , respectively, with each of the supercells containing 4 Cu₂Nb₂O₂F₁₀(bpe)₄ formula units. For the CMC simulations, the frameworks were considered rigid with atoms fixed at their DFT-optimized positions, and a fixed loading of eight sorbate molecules (per supercell) was considered, which corresponds with a loading of 1 adsorbate molecule per Cu and is about half of the maximum loading observed in experiments (Figure 2). In the canonical ensemble, the Metropolis sampling method

considered different moves, such as translation (corresponds to translation of the center-of-mass of the selected adsorbate molecule), rotation (rotating the selected adsorbate molecule), regrowth (removing a selected adsorbate molecule from the system and reintroduces it at a random position with random orientation), and conformer (collects sorbates multiple conformations), with relative probabilities of 1, 1, 0.1 and 1, respectively. Each CMC simulation included 2×10^6 loading steps, followed by 2×10^6 equilibration steps, and finally, 2×10^6 production steps to ensure reasonable ensemble averages. The output of the CMC simulations can be visualized as an isosurface (Table S11 and S12, Figures S31 and S32), encompassing the mass-middle points of all successfully inserted adsorbates during adsorbate insertion moves. The force field for the CMC simulations was parameterized as follows; the point charges for all framework atoms and adsorbates were determined via the extended charge equilibration (EQeq) method,⁴² as implemented in the RASPA.^{39,40} The Lennard-Jones (LJ) pair coefficients were taken from the Universal Force Field (UFF).^{43,44} The applied Lennard-Jones pair coefficients for framework and adsorbates are given in Table S10. The point charges used for the adsorbates are given in Figure S30, while the point charges [e] for the framework atoms are supplied in Supplementary CIF-files (AA_type_opt_with_EQeq_point_charges.cif, AB_type_opt_with_EQeq_point_charges.cif). To compute the van der Waals potentials, the Lorentz-Berthelot mixing rules were used to calculate LJ interaction parameters between unlike atoms ($\epsilon_{ij} = \sqrt{\epsilon_i \epsilon_j}$ and $\sigma_{ij} = \frac{1}{2} (\sigma_i + \sigma_j)$, where ϵ is the depth of the potential well, σ is the finite distance at which the inter-particle potential is zero).

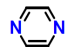
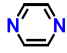
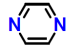
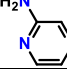
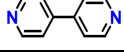
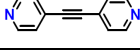
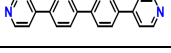
Physical and Electronic Parameters of Sorbent

Table S1. List of physical and electronic parameters for the C₃H₄, and C₃H₆.

		
Adsorbate molecules	C ₃ H ₄ (propyne)	C ₃ H ₆ (propylene)
Boiling point (K)	250	225
Dipole moment (x10 ¹⁸ / e.s.u. cm)	0.75	0.366
Polarizability (x10 ⁻²⁵ cm ³)	55.5	62.6
Kinetic diameter (Å)	4.2	4.7


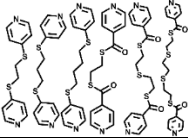
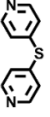
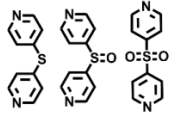
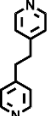
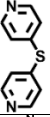
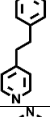
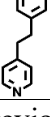
Summary of hybrid ultramicroporous materials (HUMs)

Table S2. Typical rigid bipyridine based ligands used to construct inorganic pillar based hybrid ultramicroporous materials (HUMs) with three dimensional networks.^[a]

Linker	Compound	Refcode	Year	Ref.
	SIFSIX-3-Zn	FUDQIF	2013	19
	AIFFIVE-1-Ni	DAXNOI	2017	20
	FeFIVE-1-Ni	DAXPAW	2017	20
	SIFSIX-17-Ni	UQAVAM	2021	21
	SIFSIX-1-Zn	ZESFUY	1995	22
	SIFSIX-2-Cu-i	YEMTIV	2013	19
	SIFSIX-5-Zn-i	LifWII	2011	23

[a] i = interpenetrated

Table S3. Flexible bipyridine based ligands used to construct inorganic pillar based hybrid ultramicroporous materials (HUMs) with sql coordination networks.^[b]

Linker	Compound	Layer Arrangement	Solvent	Gas Separation	Year	Ref.
	$[\text{Zn}(\text{SiF}_6)(\text{bpp})_2]_n$	Coplanar	Methanol Water	NP	2006	24
	$[\text{Zn}(\text{SiF}_6)\text{L}_2]_n$	Coplanar	EtOH CHCl_3	NP	2010	25
	$[\text{Zn}(\text{dps})_2(\text{SiF}_6)]_n$ (UTSA-300)	Coplanar	Methanol Methanol	$\text{C}_2\text{H}_2/\text{CO}_2$ $\text{C}_2\text{H}_2/\text{C}_2\text{H}_4$	2017	26
	$[\text{Cu}(\text{dps})_2(\text{SiF}_6)]$ (NCU-100 or UTSA-300-Cu)	Coplanar	Methanol Water	$\text{C}_2\text{H}_2/\text{C}_2\text{H}_4$	2020	27
	$[\text{Cu}(\text{dps})_2(\text{GeF}_6)]_n$ (GeFSIX-dps-Cu) $[\text{Zn}(\text{dps})_2(\text{GeF}_6)]_n$ (GeFSIX-dps-Zn)	Coplanar	Methanol	$\text{C}_3\text{H}_4/\text{C}_3\text{H}_6$ $\text{C}_2\text{H}_2/\text{C}_2\text{H}_4$	2020	28
	$[\text{Cu}(\text{L}1)_2(\text{NbOF}_5)]_n$ (ZUL-200) $[\text{Cu}(\text{L}2)_2(\text{NbOF}_5)]_n$ (ZUL-210) $[\text{Cu}(\text{dps})_2(\text{NbOF}_5)]_n$ (ZUL-220) $[\text{Cu}(\text{L}1)_2(\text{TiF}_6)]_n$ (ZUL-100)	Coplanar	Methanol DMF or Water	$\text{C}_2\text{H}_2/\text{C}_2\text{H}_4$	2020	29
	$[\text{Zn}(\text{SiF}_6)(\text{bpe})_2]_n$ (sql-SISIX-bpe-Zn)	Coplanar	Methanol Methanol	$\text{C}_2\text{H}_2/\text{CO}_2$ $\text{C}_2\text{H}_2/\text{C}_2\text{H}_4$	2021	30
	$[\text{Cu}(\text{dps})_2(\text{SiF}_6)]$ (SIFSIX-dps-Cu or NCU-100)	Coplanar	Methanol Water	$\text{C}_2\text{H}_2/\text{CO}_2$	2022	31
	$[\text{Cu}(\text{NbOF}_5)(\text{bpe})_2]_n$ (sql-NbOFFIVE-bpe-Cu-AA)	Coplanar	Methanol Water	$\text{C}_3\text{H}_4/\text{C}_3\text{H}_6$	-	This work
	$[\text{Cu}(\text{NbOF}_5)(\text{bpe})_2]_n$ (sql-NbOFFIVE-bpe-Cu-AB)	One layer rotated for 90°C	1,2-Dichlorobenzene Water	$\text{C}_3\text{H}_4/\text{C}_3\text{H}_6$	-	This work

[b] Abbreviations: NP = not provided; bpp = 1,3-Bis(4-pyridyl)propane; L = 1,2-bis(pyridin-4-ylthio)ethane, or 1,3-bis(pyridin-4-ylthio)propane, or 1,4-bis(pyridin-4-ylthio)butane, or S,S'-(ethane-1,2-diyl) bis(pyridine-4-carbothioate), or S,S'-(thiobis(ethane-2,1-diyl)) bis(pyridine-4-carbothioate), or S,S'-((ethane-1,2-diylbis(sulfanediy))bis(ethane-2,1-diyl)) bis(pyridine-4-

carbothioate); dps = 4,4'-dipyridylsulfide; L1 = 4,4'-dipyridylsulfone; L2 = 4,4'-dipyridylsulfoxide; bpe = 1,2-bis(4pyridyl)ethane.

Tables of Crystal Data

Table S4. Crystallographic data and refinement parameters of **pcu-NbOFFIVE-bpe-Cu**, **sql-NbOFFIVE-bpe-Cu-AA- α** and **- β** .

	pcu-NbOFFIVE-bpe-Cu	sql-NbOFFIVE-bpe-Cu-AA-α	sql-NbOFFIVE-bpe-Cu-AA-β
CCDC Number	2154469	2154470	2154471
Empirical formula	C ₂₄ H ₂₄ CuF ₅ N ₄ NbO	C ₂₆ H ₃₂ CuF ₅ N ₄ NbO ₃	C ₂₄ H ₂₄ CuF ₅ N ₄ NbO
Formula weight	635.92	700.00	635.92
Temperature/K	120	100.00	333.00(10)
Crystal system	tetragonal	monoclinic	monoclinic
Space group	<i>P4/n</i>	<i>C2/c</i>	<i>I2/m</i>
a/Å	18.6068(3)	20.1537(5)	8.5344(10)
b/Å	18.6068(3)	8.5345(2)	18.513(2)
c/Å	8.3522(2)	19.4208(4)	9.5971(11)
α /°	90	90	90
β /°	90	117.2220(10)	96.835(11)
γ /°	90	90	90
Volume/Å ³	2891.64(12)	2970.43(12)	1505.5(3)
Z	2	4	2
$\rho_{\text{calc}}/\text{cm}^3$	0.730	1.565	1.403
μ/mm^{-1}	0.593	4.608	1.138
Radiation	Mo K α	Cu K α	Mo K α
Reflections collected	43292	12499	12846
Independent reflections	3531	2287	1379
Goodness-of-fit on F ²	1.079	1.079	1.046
R ₁ [I > 2 σ (I)] ^[c]	0.0825	0.0554	0.0792
wR ₂ [I > 2 σ (I)] ^[d]	0.2765	0.1627	0.2445

$$[c] R_1 = \Sigma||F_o| - |F_c||/\Sigma|F_o|. \quad [d] wR_2 = \{\Sigma[w(F_o^2 - F_c^2)^2]/\Sigma[w(F_o^2)^2]\}^{1/2}$$

Table S5. Crystallographic data and refinement parameters of **sql-NbOFFIVE-bpe-AB- α** phase and **- β_1** phase.

	sql-NbOFFIVE-bpe-AB- α	sql-NbOFFIVE-bpe-AB- β_1	sql-NbOFFIVE-bpe-AB- β_1 (Synchrotron)
CCDC Number	2154472	2154473	1973753
Empirical formula	C ₂₄ H ₂₄ CuF ₅ N ₄ NbO	C ₂₄ H ₂₄ CuF ₅ N ₄ NbO	C ₂₄ H ₂₆ CuF ₅ N ₄ NbO ₂
Formula weight	635.92	635.92	653.94
Temperature/K	295.0(2)	293(2)	293(2)
Crystal system	tetragonal	tetragonal	tetragonal
Space group	<i>P4₂/mmc</i>	<i>P4₂/mnm</i>	<i>P4₂/mnm</i>
a/Å	9.0177(7)	12.5384(7)	12.40990(10)
b/Å	9.0177(7)	12.5384(7)	12.40990(10)
c/Å	18.9558(15)	18.7936(12)	18.8877(3)
α /°	90	90	90
β /°	90	90	90
γ /°	90	90	90
Volume/Å ³	1541.5(3)	2954.6(4)	2908.81(7)
Z	2	4	4
$\rho_{\text{calc}}/\text{cm}^3$	1.37	1.43	1.493
μ/mm^{-1}	4.337	1.16	1.141
Radiation	Cu K α	Mo K α	Synchrotron
Reflections collected	3988	30190	81311
Independent reflections	894	1502	5243
Goodness-of-fit on F ²	1.081	1.098	0.992
R ₁ [I>2 σ (I)] ^[c]	0.0856	0.0998	0.0624
wR ₂ [I>2 σ (I)] ^[d]	0.2632	0.2436	0.2372

$$[c] R_1 = \Sigma||F_o| - |F_c||/\Sigma|F_o|. \quad [d] wR_2 = \{\Sigma[w(F_o^2 - F_c^2)^2]/\Sigma[w(F_o^2)^2]\}^{1/2}.$$

Optical Image

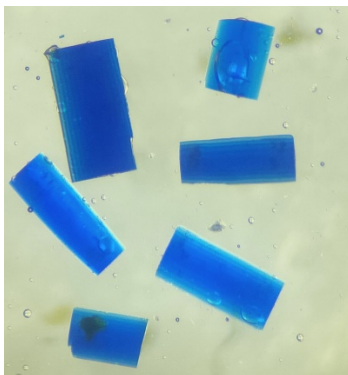


Figure S1. Optical image of as-synthesized **sql-NbOFFIVE-bpe-Cu-AA- α** .

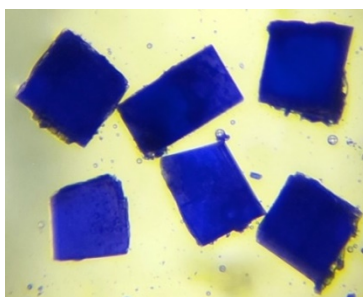


Figure S2. Optical image of as-synthesized **sql-NbOFFIVE-bpe-Cu-AB- α** .

Crystal Structures

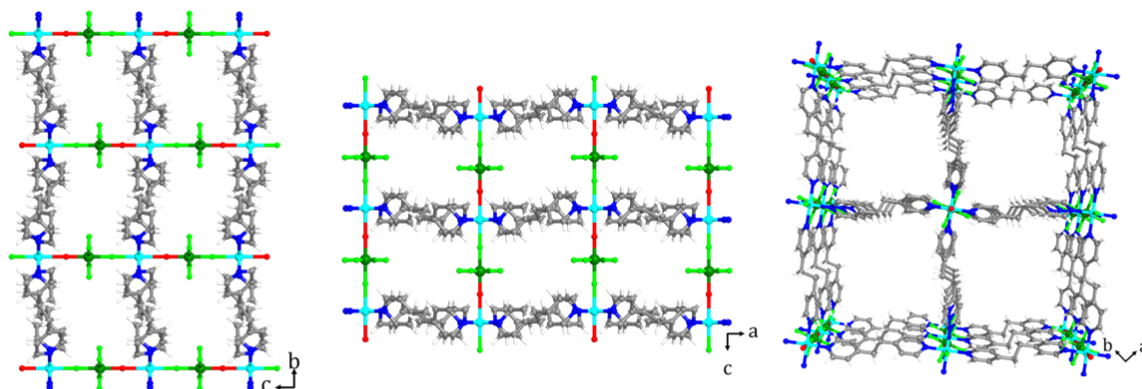


Figure S3. Structural representations of **pcu-NbOFFIVE-bpe-Cu**, a 3D non-interpenetrated network, across different planes.

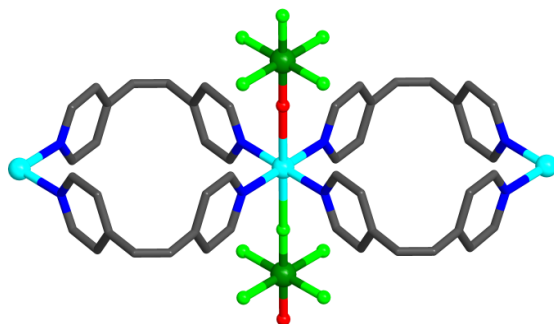


Figure S4. Coordination environment of Cu^{2+} cation in the structures of **sql-NbOFFIVE-bpe-Cu-AA- α** and **sql-NbOFFIVE-bpe-Cu-AB- α** .

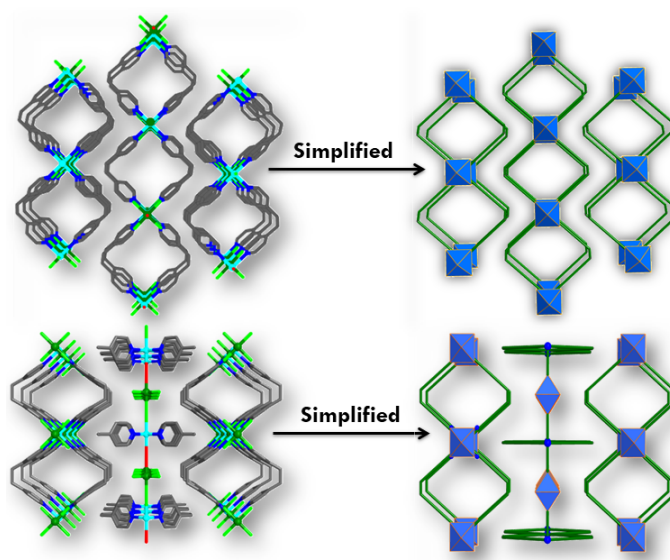


Figure S5. Simplified structures of **sql-NbOFFIVE-bpe-Cu-AA- α** (above array) and **sql-NbOFFIVE-bpe-Cu-AB- α** (below array).

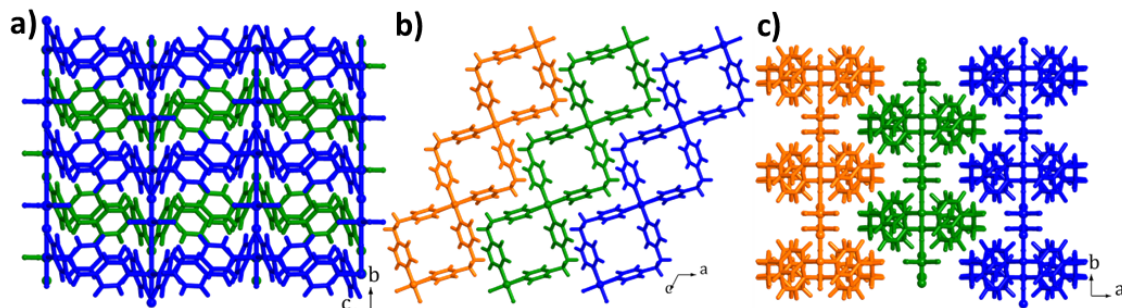


Figure S6. Packing structures for **sql-NbOFFIVE-bpe-Cu-AA- α** along with the [100], [010], and [001] direction, respectively.

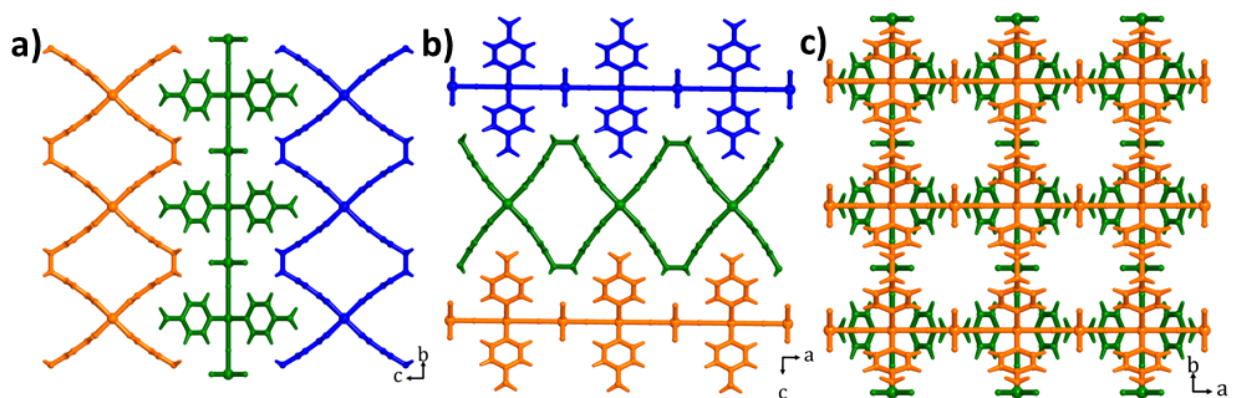


Figure S7. Packing structures for **sql-NbOFFIVE-bpe-Cu-AB- α** along with the [100], [010], and [001] direction, respectively.

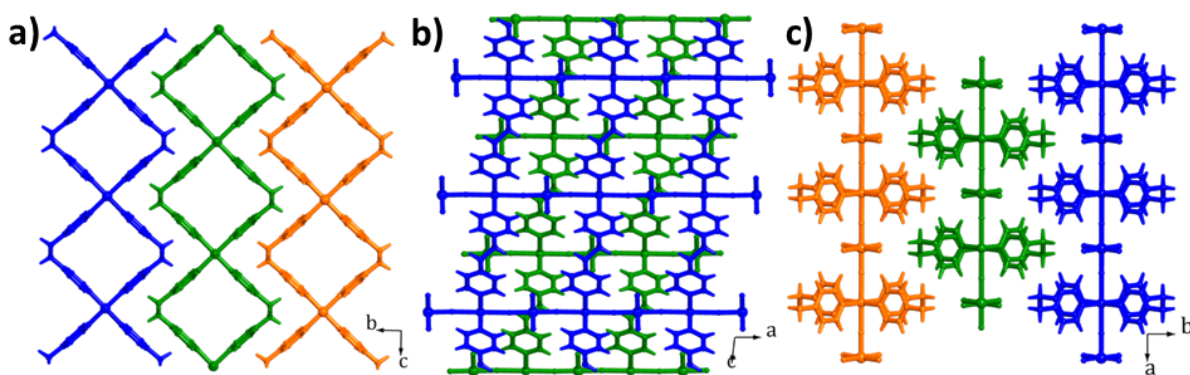


Figure S8. Packing structures of **sql-NbOFFIVE-bpe-Cu-AA- β** along with the [100], [010], and [001] direction, respectively.

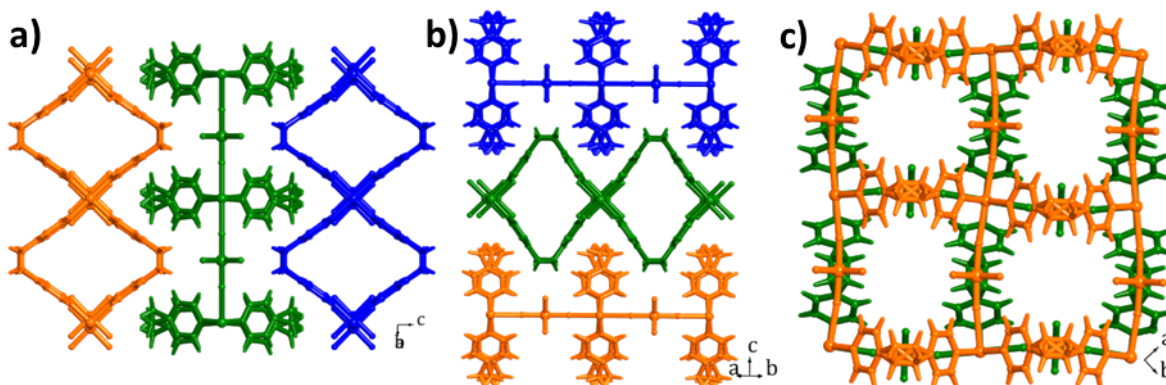


Figure S9. Packing structures of **sql-NbOFFIVE-bpe-Cu-AB- β_1** along with the $[1\bar{1}0]$, $[110]$, and [001] direction, respectively.

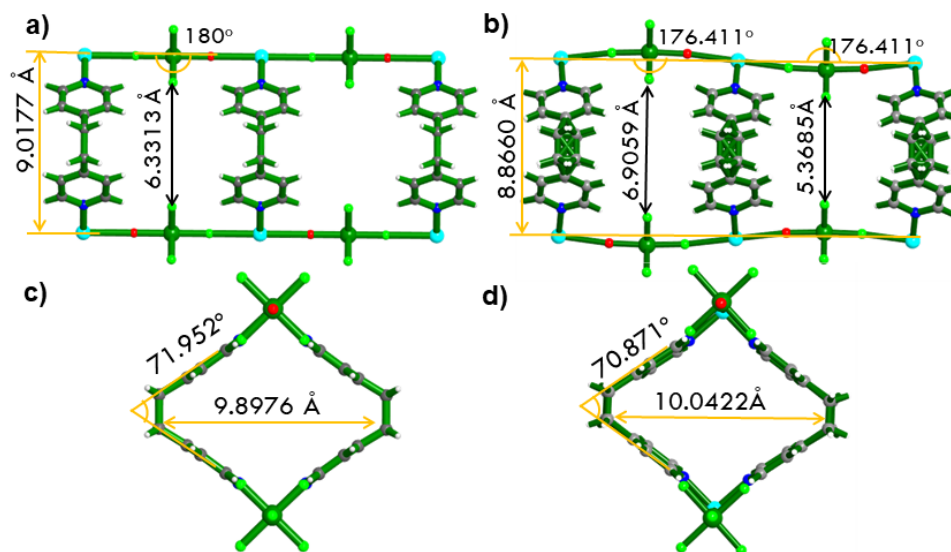


Figure S10. Comparison of different phases for **sql-NbOFFIVE-bpe-Cu-AB- α** (a, c) and **sql-NbOFFIVE-bpe-AB- β_1** (b, d) (Van der Waals radius is included for the distance measurements).

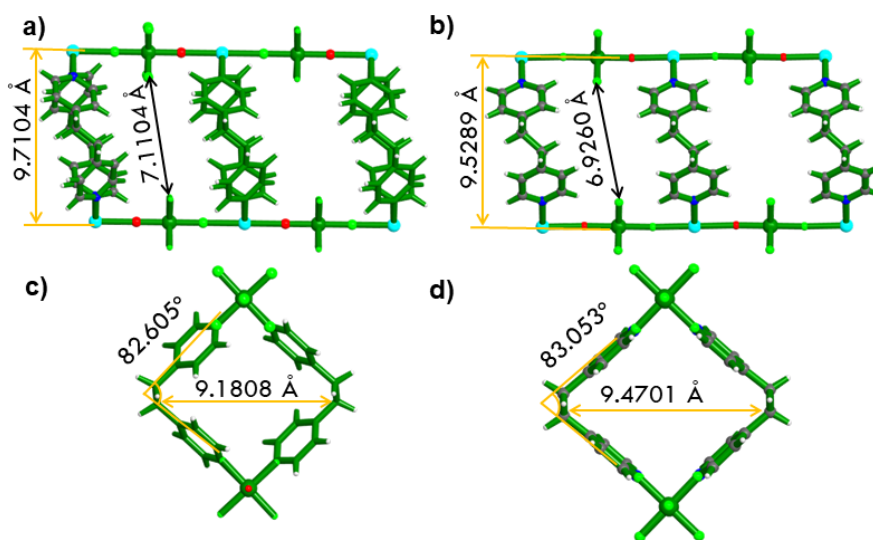


Figure S11. Comparison of Packing modes for **sql-NbOFFIVE-bpe-Cu-AA- α** (a, c) and **sql-NbOFFIVE-bpe-Cu-AA- β** (b, d) (Van der Waals radius is included for the distance measurements).

PXRD Patterns

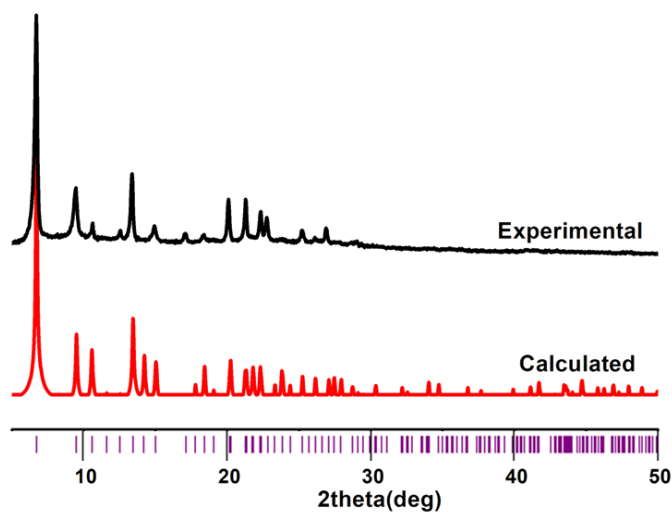


Figure S12. PXRD patterns of as-synthesized sample **pcu-NbOFFIVE-bpe-Cu**, along with the calculated XRD pattern from the single-crystal X-ray structure.

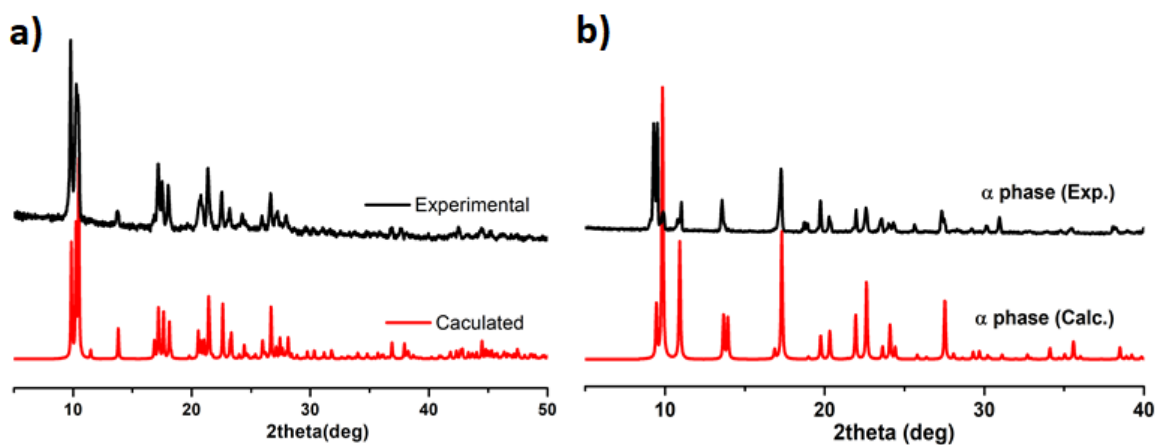


Figure S13. PXRD patterns of as-synthesized sample **sql-NbOFFIVE-bpe-Cu-AA- α** (a) and **sql-NbOFFIVE-bpe-Cu-AB- α** (b), along with the simulated XRD pattern from the single-crystal X-ray structure.

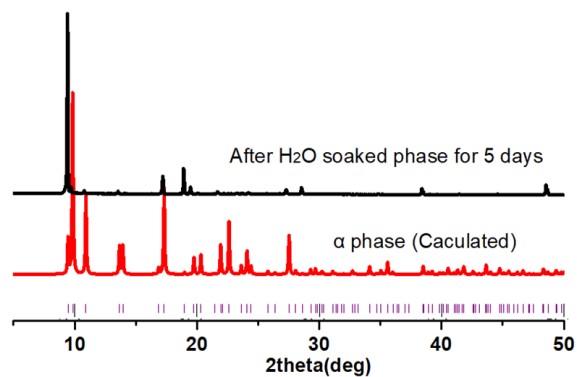


Figure S14. Comparison of experimental and calculated PXRD patterns of **sql-NbOFFIVE-bpe-Cu-AB- α** and water-soaked phase.

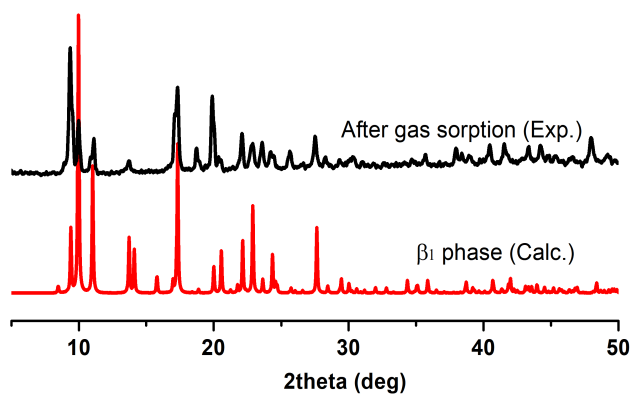


Figure S15. Comparison of PXRD patterns for **sql-NbOFFIVE-bpe-Cu-AB** after gas sorption and calculated β_1 phase.

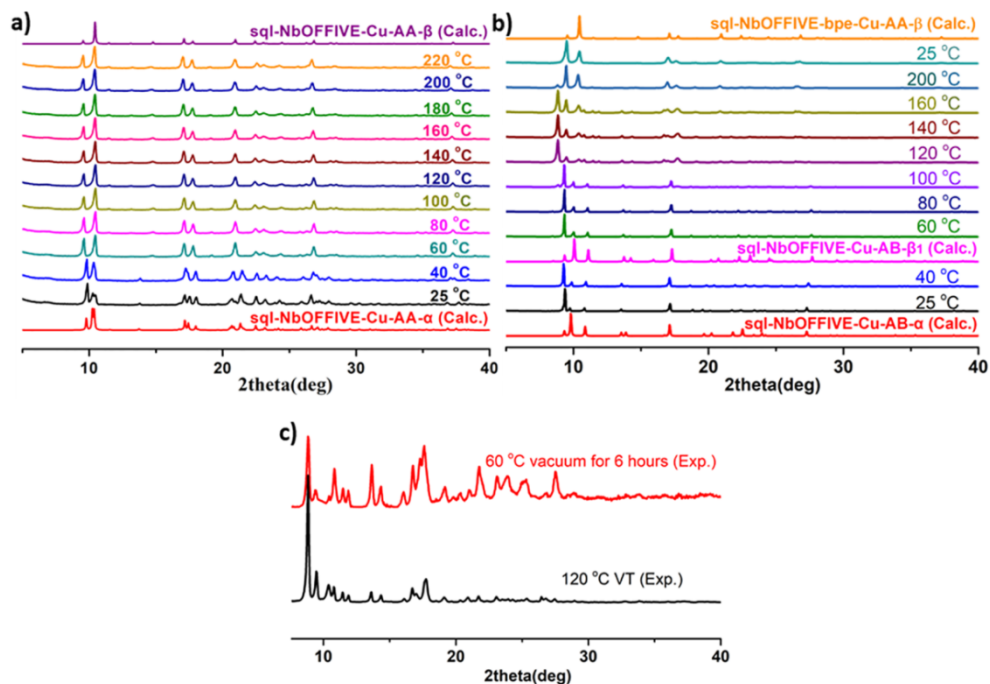


Figure S16. Variable temperature PXRD patterns for MeOH exchanged **sql-NbOFFIVE-bpe-Cu-AA** (a), **sql-NbOFFIVE-bpe-Cu-AB** (b), and comparison of PXRD patterns for MeOH exchanged **sql-NbOFFIVE-bpe-Cu-AB** after heating the sample at 60 °C under vacuum for 6 hours with VT-PXRD pattern at 120 °C (c).

TGA Curves

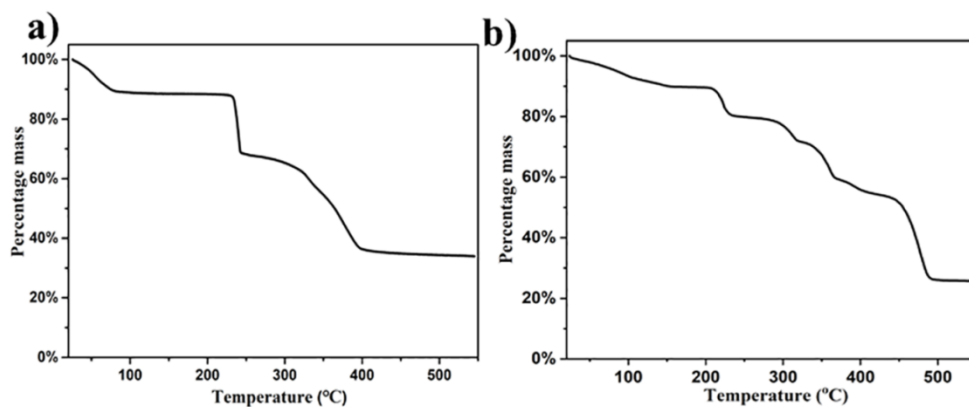
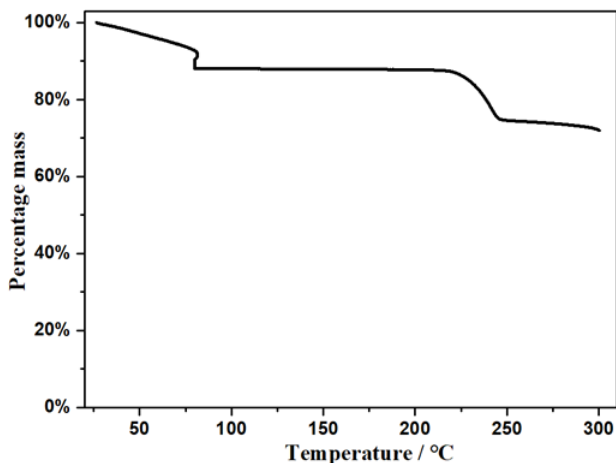


Figure S17. Thermogravimetric analysis profile of the as-synthesized sample **sql-NbOFFIVE-bpe-Cu-AA-α** (a) and **sql-NbOFFIVE-bpe-Cu-AB-α** (b).



Procedure:

- Step 1: Ramp 10.00 °C/min to 80.00 °C
- Step 2: Isothermal for 120.00 min
- Step 3: Mark end of cycle 1
- Step 4: Ramp 10.00 °C/min to 140.00 °C
- Step 5: Isothermal for 30.00 min
- Step 6: Mark end of cycle 2
- Step 7: Ramp 20.00 °C/min to 300.00 °C
- Step 8: Isothermal for 5.00 min
- Step 9: Mark end of cycle 3
- Step 10: Ramp 20.00 °C/min to 25.00 °C
- Step 11: Mark end of cycle 4

Figure S18. Thermogravimetric analysis profile of MeOH exchanged sample **sql-NbOFFIVE-bpe-Cu-AB- α** with different procedure.

Sorption Studies

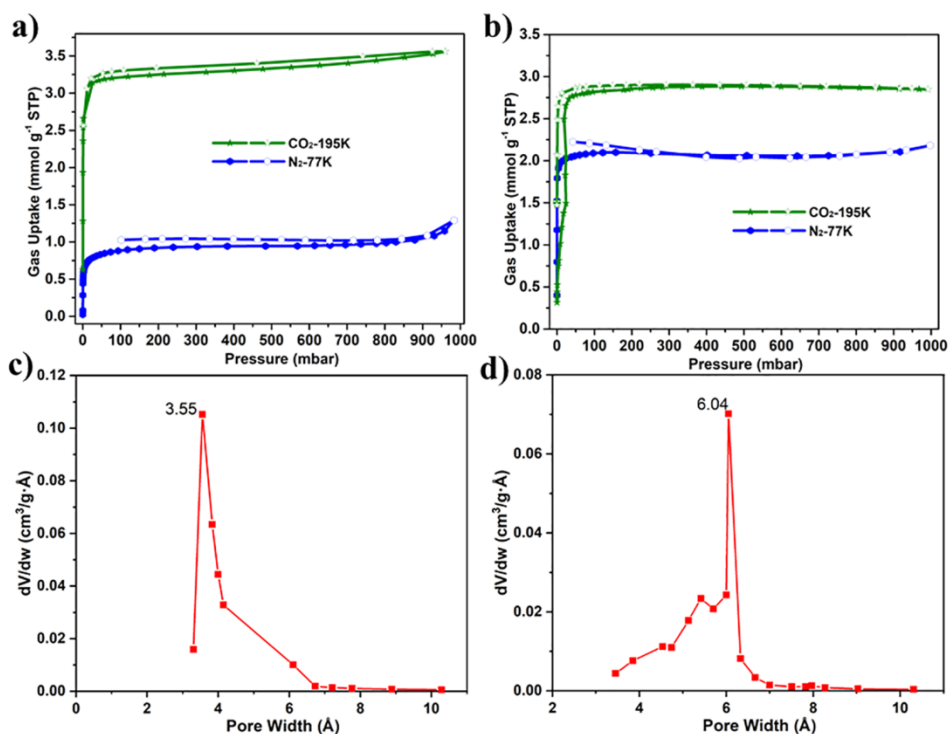


Figure S19. Low-temperature CO₂ and N₂ sorption isotherms of **sql-NbOFFIVE-bpe-Cu-AA** (a) and **sql-NbOFFIVE-bpe-Cu-AB** (b); Horvath-Kawazoe pore size distribution of **sql-NbOFFIVE-bpe-Cu-AA** (c) and **sql-NbOFFIVE-bpe-Cu-AB** (d) derived from 195 K CO₂.

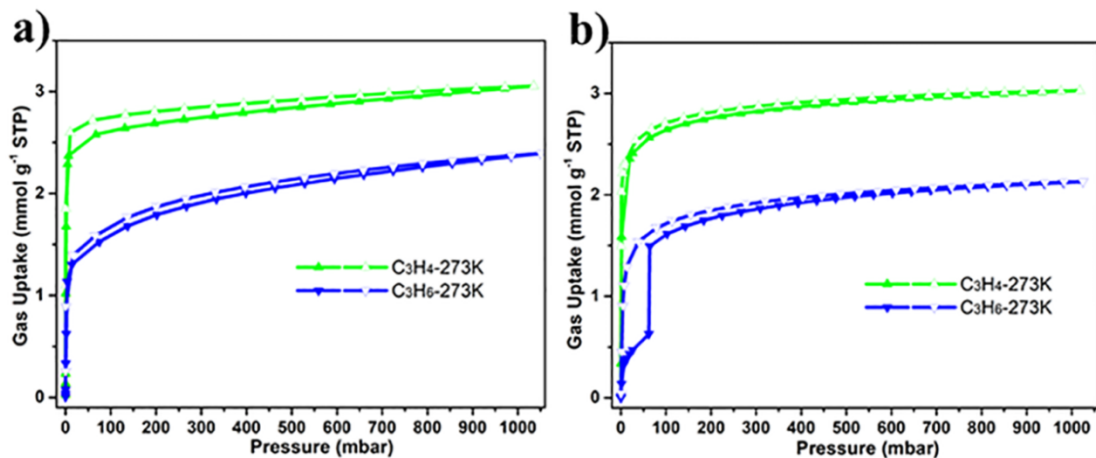


Figure S20. C₃H₄ and C₃H₆ adsorption isotherms of **sql-NbOFFIVE-bpe-Cu-AA** (a) and **sql-NbOFFIVE-bpe-Cu-AB** (b) at 273 K.

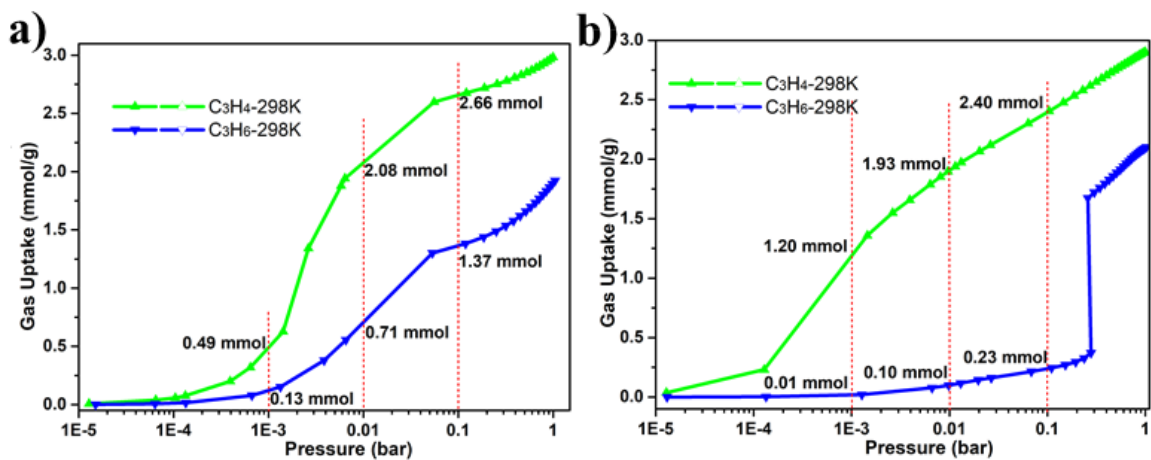


Figure S21. Log scale plot of single-component (C₃H₄ and C₃H₆) gas adsorption isotherms of **sql-NbOFFIVE-bpe-Cu-AA** (a) and **sql-NbOFFIVE-bpe-Cu-AB** (b) at 298 K (0-1 bar).

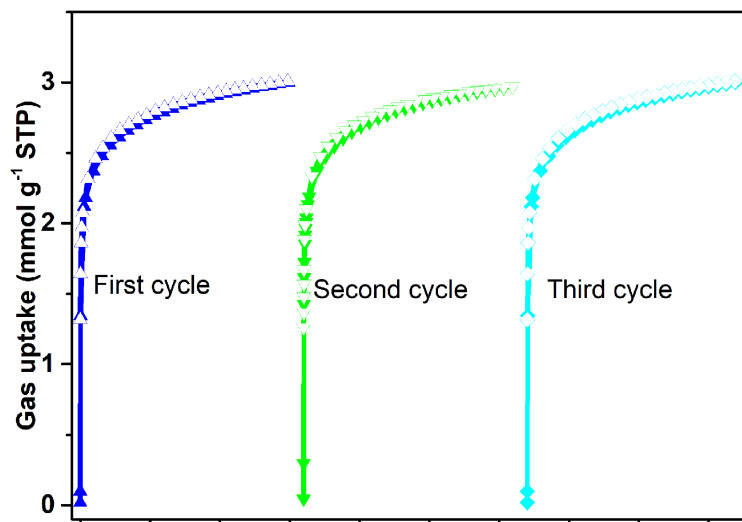


Figure S22. Three cycles of C₃H₄ adsorption and desorption on **sql-NbOFFIVE-bpe-Cu-AB** at 298 K (0-1 bar).

Fitting Isotherms

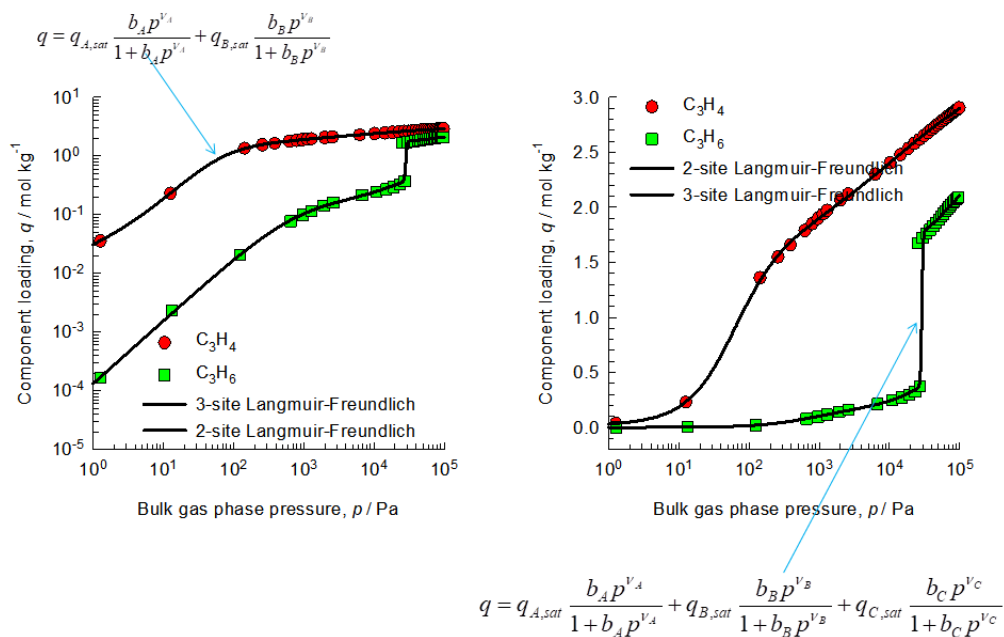


Figure S23. Fitting unary isotherms of C₃H₄ and C₃H₆ for **sql-NbOFFIVE-bpe-Cu-AB** at 298 K.

IAST selectivity

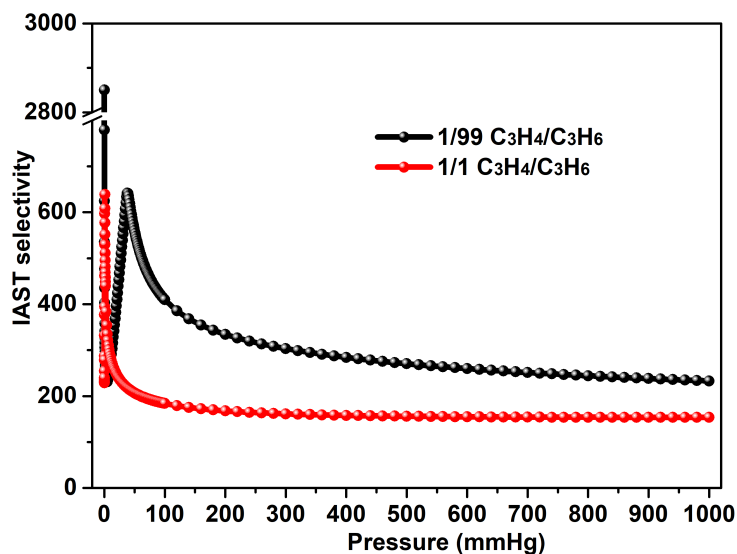


Figure S24. IAST selectivity of **sql-NbOFFIVE-bpe-Cu-AB** calculated for C_3H_4/C_3H_6 gas mixtures for 1:1 and 1:99 ratios at 298 K.

Fitting Related Parameter

Table S6. 2-site Langmuir-Freundlich parameter fits for C_3H_4 .

$q_{A,sat} / \text{mol kg}^{-1}$	1.46
$q_{B,sat} / \text{mol kg}^{-1}$	2
$b_A / \text{Pa}^{-\nu_A}$	3.691E-03
$b_B / \text{Pa}^{-\nu_B}$	1.292E-02
$\nu_A / \text{dimensionless}$	1.36
$\nu_B / \text{dimensionless}$	0.46

Table S7. 3-site Langmuir-Freundlich parameter fits for C_3H_6 .

$q_{A,sat} / \text{mol kg}^{-1}$	1.39
$q_{B,sat} / \text{mol kg}^{-1}$	0.18

$q_{C,sat} / \text{mol kg}^{-1}$	1.2
$b_A / \text{Pa}^{-\nu_A}$	1.153E-245
$b_B / \text{Pa}^{-\nu_B}$	7.128E-04
$b_C / \text{Pa}^{-\nu_C}$	2.584E-06
$\nu_A / \text{dimensionless}$	54.9
$\nu_B / \text{dimensionless}$	1.072
$\nu_C / \text{dimensionless}$	1.1

Experimental Breakthrough Related Data

Table S8. The data related to breakthrough measurement for **sql-NbOFFIVE-bpe-Cu-AB** at 1.0 bar and 298 K.

	sql-NbOFFIVE-bpe-Cu-AB
C ₃ H ₄ inlet flow (cc min ⁻¹)	0.01
C ₃ H ₆ inlet flow (cc min ⁻¹)	0.99
C ₃ H ₄ uptake (mmol g ⁻¹)	1.20
C ₃ H ₆ uptake (mmol g ⁻¹)	0.44
C ₃ H ₆ productivity (mmol g ⁻¹)	118
α_{AC}	270
Minimum effluent C ₃ H ₆ purity	99.99%

Gravimetric Kinetics

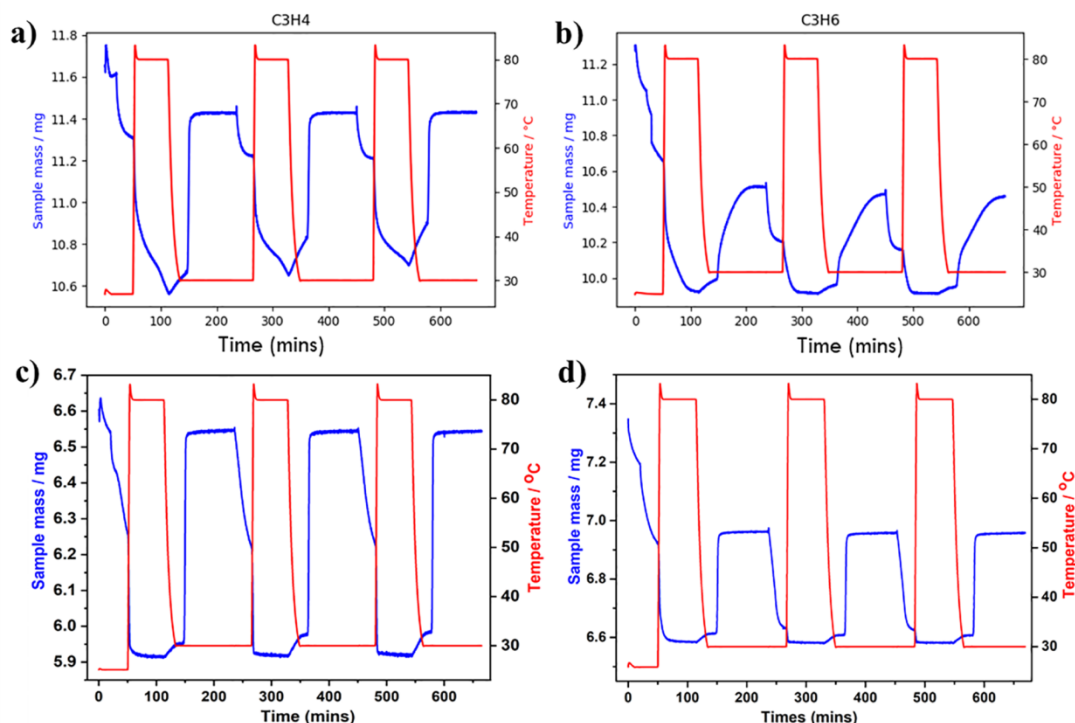


Figure S25. C₃H₄ and C₃H₆ adsorption kinetics plot at different temperatures and 1.0 bar for **sql-NbOFFIVE-bpe-Cu-AB** (a, b) and **sql-NbOFFIVE-bpe-Cu-AA** (c, d).

Gravimetric uptakes were recorded under pure C₃H₄ and C₃H₆ flows using TGA instrument TA Q50 V20.13 with sample mass 11.6540 mg and 11.3050 mg for **sql-NbOFFIVE-bpe-Cu-AB**, as well as 6.6080 mg and 7.3480 mg for **sql-NbOFFIVE-bpe-Cu-AA**, respectively. C₃H₄ and C₃H₆ flow rates of 10 cm³/min were used in these experiments, and gas flows were controlled by pre-calibrated Bronkhorst Mass Flow Controllers. Desorption at 353 K was performed under N₂ flow of 60 cm³ /min. The data was evaluated using the T.A. Universal Analysis suite for Windows. The procedure we used is listed as follows.

Step	Action	Step	Action
1	Select gas 2	23	Isothermal for 30.00 min
2	Mass flow 60.00 mL/min	24	Mark end of cycle 3

3	Isothermal for 20.00 min	25	Select gas 2
4	Mark end of cycle 0	26	Mass flow 10.00 mL/min
5	Select gas 1	27	Isothermal for 90.00 min
6	Mass flow 60.00 mL/min	28	Mark end of cycle 4
7	Isothermal for 30.00 min	29	Select gas 1
8	Ramp 20.00 °C/min to 80.00 °C	30	Mass flow 60.00 mL/min
9	Isothermal for 60.00 min	31	Isothermal for 30.00 min
10	Ramp 20.00 °C/min to 30.00 °C	32	Ramp 20.00 °C/min to 80.00 °C
11	Isothermal for 30.00 min	33	Isothermal for 60.00 min
12	Mark end of cycle 1	34	Ramp 20.00 °C/min to 30.00 °C
13	Select gas 2	35	Isothermal for 30.00 min
14	Mass flow 10.00 mL/min	36	Mark end of cycle 5
15	Isothermal for 90.00 min	37	Select gas 2
16	Mark end of cycle 2	38	Mass flow 10.00 mL/min
17	Select gas 1	39	Isothermal for 90.00 min
18	Mass flow 60.00 mL/min	40	Mark end of cycle 6
19	Isothermal for 30.00 min	41	Select gas 1
20	Ramp 20.00 °C/min to 80.00 °C	42	Mass flow 10.00 mL/min
21	Isothermal for 60.00 min	43	Mark end of cycle 8
22	Ramp 20.00 °C/min to 30.00 °C		

Note: gas 2 is target gas (C₃H₄ or C₃H₆); gas 1 is N₂.

Water Sorption

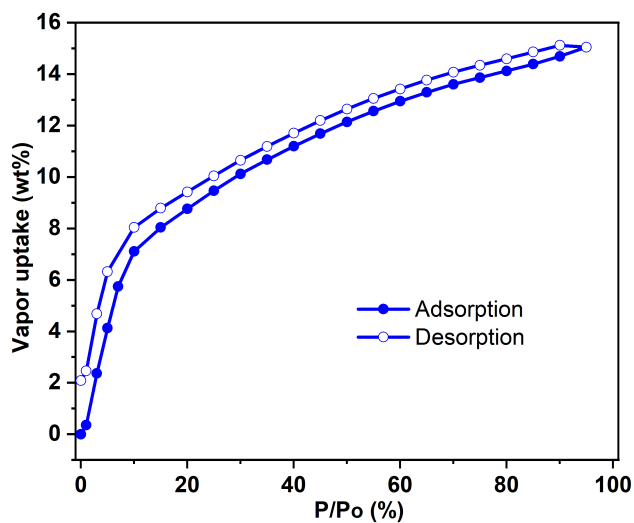


Figure S26. Water vapor sorption isotherm of **sql-NbOFFIVE-bpe-Cu-AB** at 298 K.

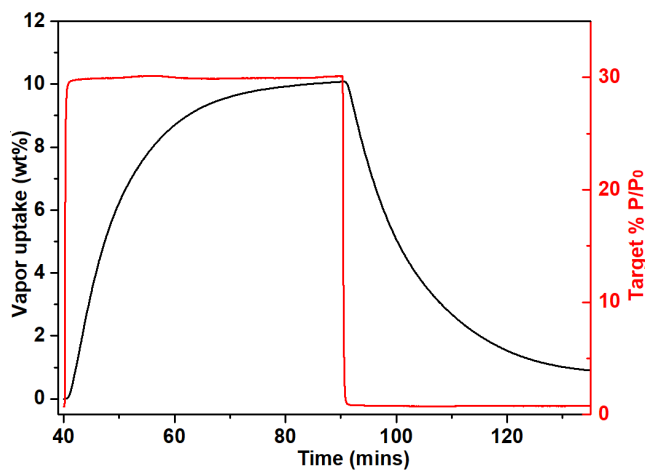


Figure S27. Vapor adsorption kinetics plot of **sql-NbOFFIVE-bpe-Cu-AB** at 298 K.

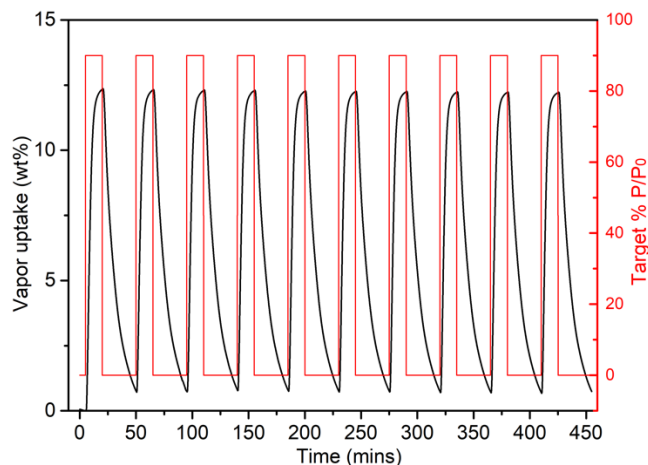


Figure S28. Adsorption-desorption cycles for **sql-NbOFFIVE-bpe-Cu-AB** at 298 K (adsorption at 90% RH and desorption at 0 RH).

Experimental Setup of DCB

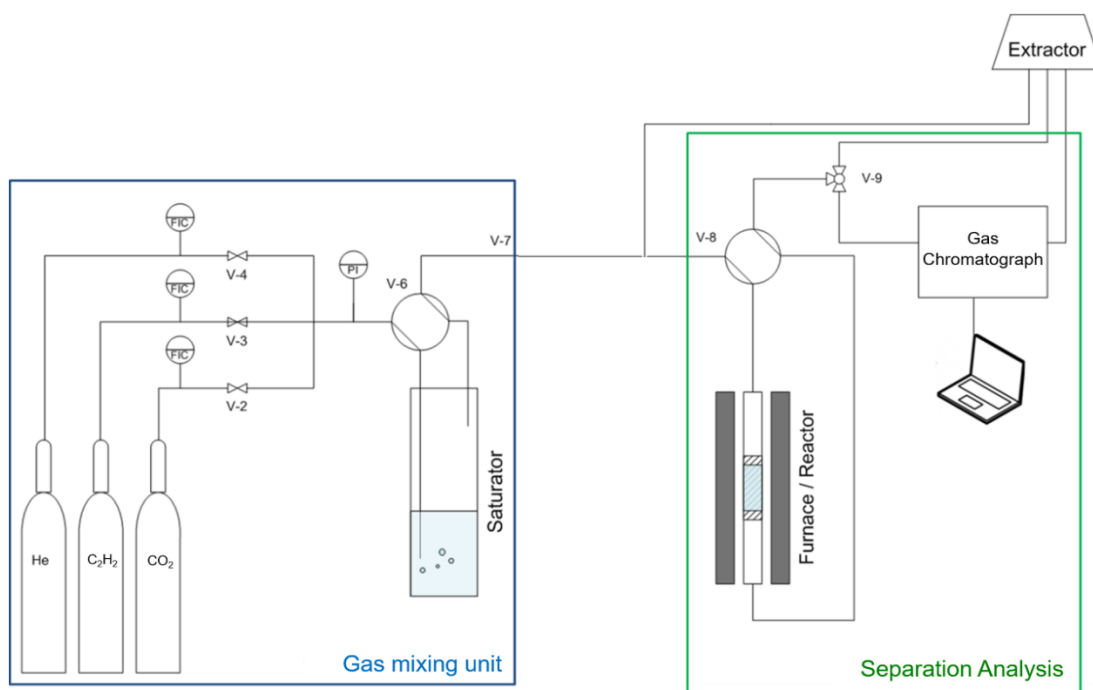


Figure S29. Schematic of dynamic gas breakthrough separation experimental setup, including gas mixing unit, gravimetric gas uptake analyser and gas separation analyser.³²

Modeling Studies

Table S9. Details on the binding sites (two possible orientations of the adsorbates), obtained from DFT calculations.

Adsorbent	Adsorbate	File Name	Adsorption enthalpy (kJ mol ⁻¹)	Adsorption Enthalpy	Distance (Å)
sql-NbOFFIVE-bpe-Cu-AA	C ₃ H ₄	sql-NbOFFIVE-bpe-Cu-AA-C ₃ H ₄ binding site	-62.7	C-H...F	2.49, 2.60, 2.88, 2.61
				C-H(Ligand)...π(C ₃ H ₄)	2.98
	C ₃ H ₆	sql-NbOFFIVE-bpe-Cu-AA-C ₃ H ₆ binding site	-65.2	C-H...F	2.50, 2.43, 2.58, 2.76
				C-H(Ligand)...π(C ₃ H ₆)	3.09
sql-NbOFFIVE-bpe-Cu-AB	C ₃ H ₄	sql-NbOFFIVE-bpe-Cu-AB-C ₃ H ₄ binding site	-69.0	C-H...F	2.35, 2.36
				C-H(Ligand)...π(C ₃ H ₄)	2.77, 3.04, 2.85, 3.10, 3.09 (with another layer)
	C ₃ H ₆	sql-NbOFFIVE-bpe-Cu-AB-C ₃ H ₆ binding site	-53.0	C-H...F	2.64, 2.83, 2.91, 2.79, 2.43, 2.64, 2.93, 2.85
				C-H(Ligand)...π(C ₃ H ₆)	No

Table S10. Lennard-Jones (LJ) interaction parameters representing framework atoms. The interaction with the sorbate molecules was calculated using Lorentz-Berthelot mixing rules.

Atom	ε/k _B [K]	σ [Å]
Nb	29.68992	2.819694
Cu	2.516095	3.113691
F	25.16095	2.996983

O	30.19314	3.118146
N	34.72211	3.260689
C	52.83799	3.430851
H	22.14164	2.571134
C_3H_4 and C_3H_6		
C	52.83799	3.430851
H	22.14164	2.571134

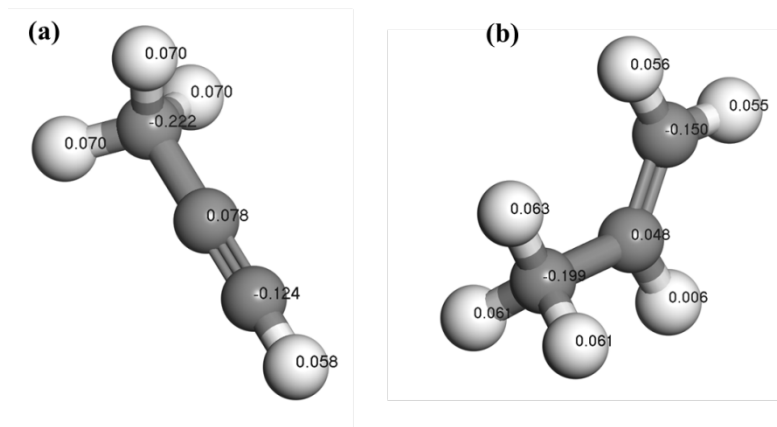


Figure S30. Atomic structures and point charges [e] of (a) C_3H_4 and (b) C_3H_6 .

Table S11. Visualization from different view angles of C_3H_4 and C_3H_6 binding site isosurfaces from CMC simulations with 8 adsorbates in a $1 \times 2 \times 1$ **sql-NbOFFIVE-bpe-Cu-AA- α** supercell.

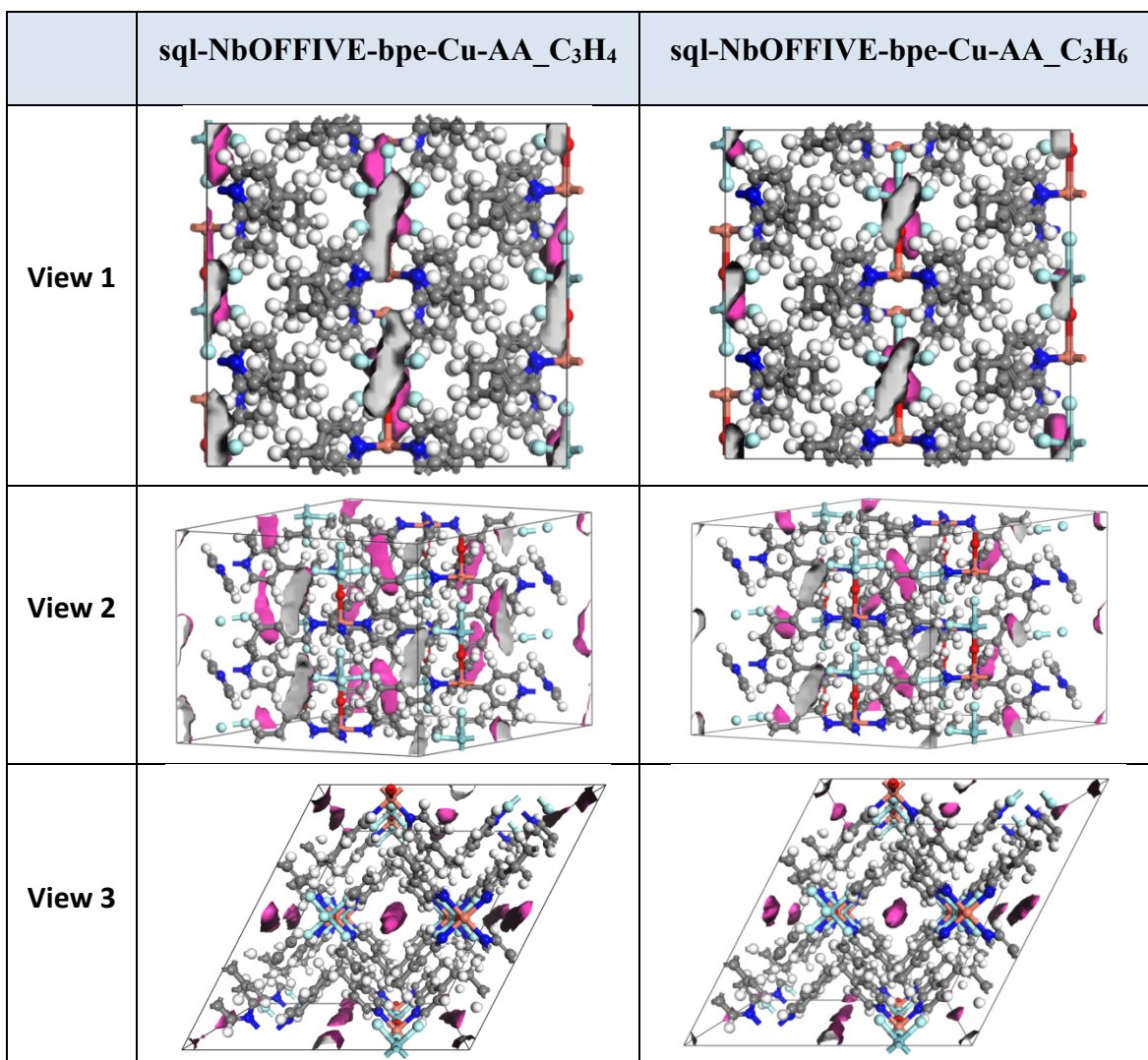
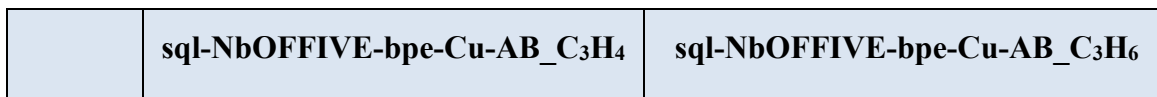
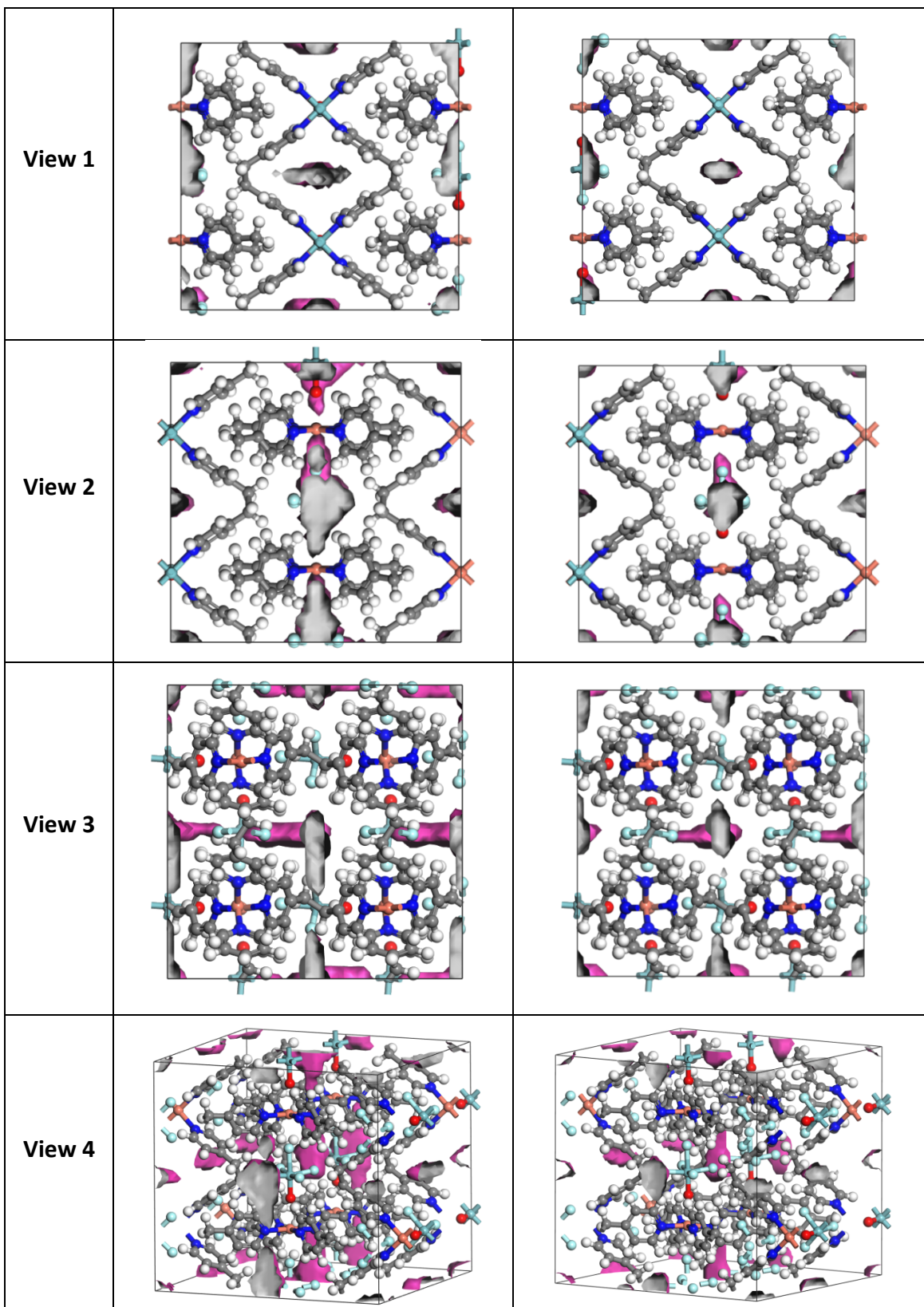


Table S12. Visualization from different view angles of C_3H_4 and C_3H_6 binding site isosurfaces from CMC simulations with 8 adsorbates in a $2 \times 2 \times 1$ **sql-NbOFFIVE-bpe-Cu-AB- α** supercell.





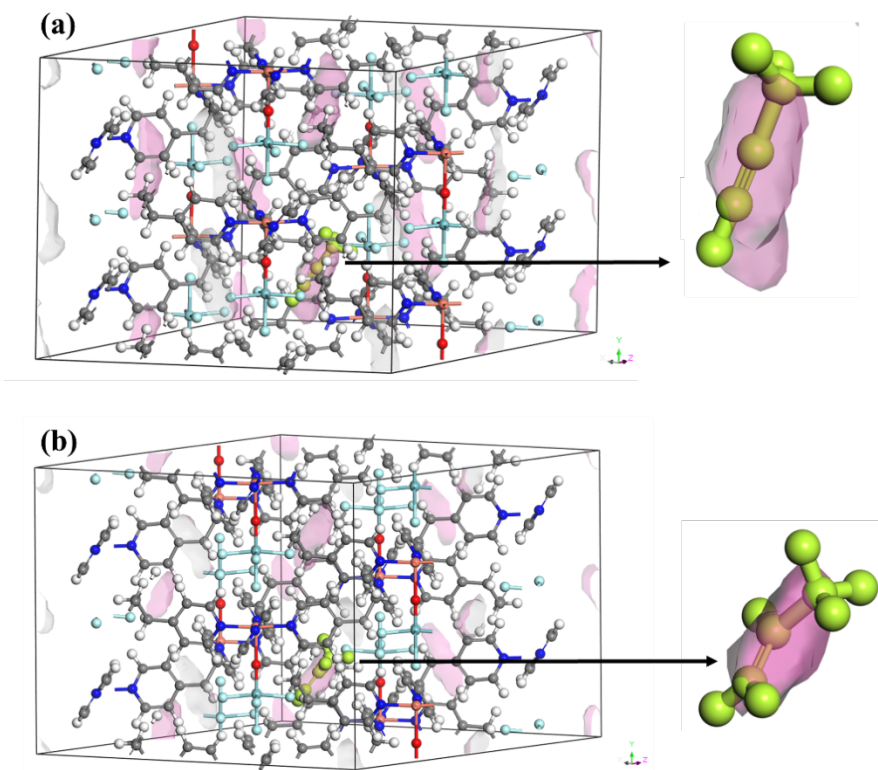


Figure S31. Visualization binding sites of (a) C_3H_4 and (b) C_3H_6 by CMC (pink isosurfaces) and DFT (light green ball and stick model) for **sql-NbOFFIVE-bpe-Cu-AA- α** framework.

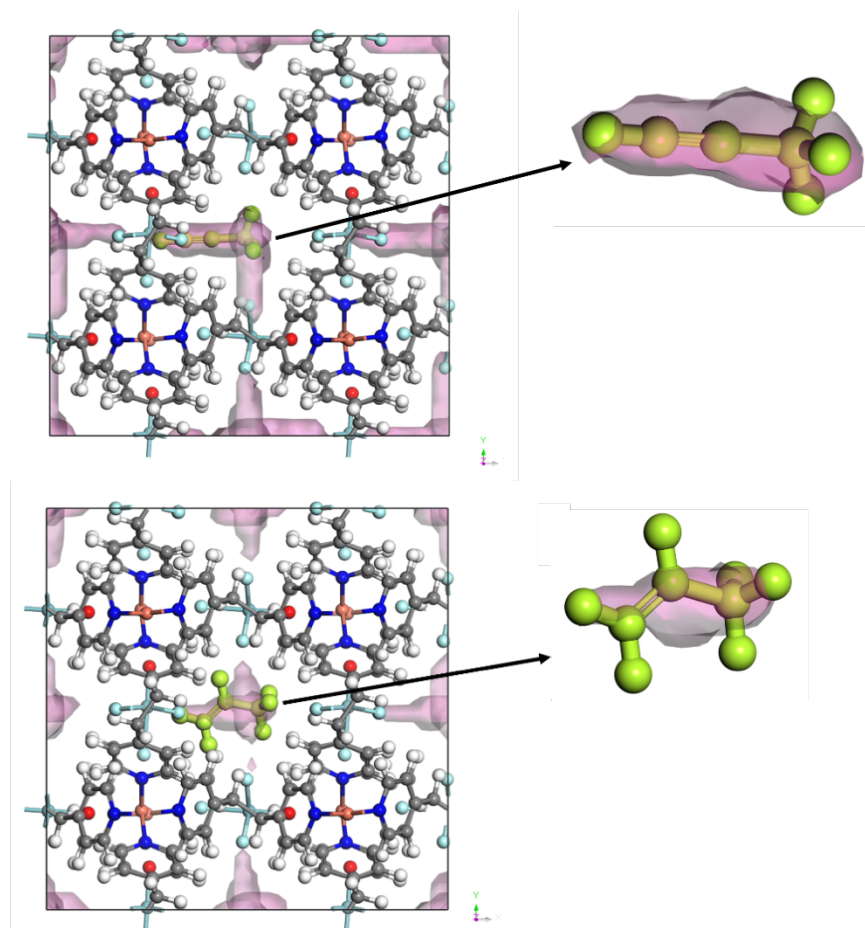


Figure S32. Visualization binding sites of (a) C_3H_4 and (b) C_3H_6 by CMC (pink isosurfaces) and DFT (light green ball and stick model) for **sqI-NbOFFIVE-bpe-Cu-AB- α** framework.

Notation

b	Langmuir-Freundlich constant, $\text{Pa}^{-\nu}$
m_{ads}	mass of adsorbent in fixed bed, kg
p	pressure, Pa
q	component molar loading, mol kg^{-1}
q_{sat}	saturation loading, mol kg^{-1}

Q_0 volumetric flow rate of gas mixture at inlet to fixed bed, L s⁻¹

Greek letters

ν Freundlich exponent, dimensionless

τ time, dimensionless

References

- [1] Bondi, A. van der Waals Volumes and Radii. *J. Phys. Chem. A*. **1964**, *68*, 441-451.
- [2] Krause, L.; Herbst-Irmer, R.; Sheldrick, G. M.; Stalke, D. Comparison of silver and molybdenum microfocus x-ray sources for single-crystal structure determination. *J Appl Crystallogr.* **2015**, *48*, 3-10.
- [3] Gannon, R. E.; Krukonis, V. J.; Schoenberg, T. Conversion of Coal to Acetylene in Arc-Heated Hydrogen. *Product R&D*. **1970**, *9*, 343-347.
- [4] Sheldrick, G. SHELXT - Integrated space-group and crystal-structure determination. *Acta Crystallogr. A*. **2015**, *71*, 3-8.
- [5] Sheldrick, G. Crystal structure refinement with SHELXL. *Acta Crystallogr. Sect. C*. **2015**, *71*, 3-8.
- [6] Dolomanov, O. V.; Bourhis, L. J.; Gildea, R. J.; Howard, J. A. K.; Puschmann, H. OLEX2: a complete structure solution, refinement and analysis program. *J Appl Crystallogr.* **2009**, *42*, 339-341.
- [7] Spackman, P. R.; Turner, M. J.; McKinnon, J. J.; Wolff, S. K.; Grimwood, D. J.; Jayatilaka, D.; Spackman, M. A. CrystalExplorer: a program for Hirshfeld surface analysis,

visualization and quantitative analysis of molecular crystals. *J. Appl. Crystallogr.* **2021**, *54*, 1006-1011.

[8] Peng, Y. L.; Wang, T.; Jin, C.; Li, P.; Suepaul, S.; Beemer, G.; Chen, Y.; Krishna, R.; Cheng, P.; Pham, T.; Space, B.; Zaworotko, M. J.; Zhang, Z. A robust heterometallic ultramicroporous MOF with ultrahigh selectivity for propyne/propylene separation. *J. Mater. Chem. A* **2021**, *9*, 2850-2856.

[9] Gutierrez-Sevillano, J. J.; Calero, S.; Krishna, R. Separation of benzene from mixtures with water, methanol, ethanol, and acetone: highlighting hydrogen bonding and molecular clustering influences in CuBTC. *Phys. Chem. Chem. Phys.* **2015**, *17*, 20114-24.

[10] Gutiérrez-Sevillano, J. J.; Calero, S.; Krishna, R. Selective adsorption of water from mixtures with 1-alcohols by exploitation of molecular packing effects in CuBTC. *J. Phys. Chem. C* **2015**, *119*, 3658-3666.

[11] PRAUSNITZ, A. L. M. a. J. M. Thermodynamics of mixed-gas adsorption. *AIChE. J.* **1965**, *11*, 121-127.

[12] Krishna, R. The Maxwell-stefan description of mixture diffusion in nanoporous crystalline materials. *Microporous Mesoporous Mater.* **2014**, *185*, 30-50.

[13] Krishna, R. Methodologies for evaluation of metal-organic frameworks in separation applications. *RSC Adv.* **2015**, *5*, 52269-52295.

[14] Krishna, R. Screening Metal-Organic Frameworks for mixture separations in fixed-bed adsorbers using a combined selectivity/capacity metric. *RSC Adv.* **2017**, *7*, 35724-35737.

[15] Krishna, R. Methodologies for screening and selection of crystalline microporous materials in mixture separations. *Sep. Purif. Technol.* **2018**, *194*, 281-300.

- [16] Krishna, R. Metrics for evaluation and screening of metal-organic frameworks for applications in mixture separations. *ACS Omega*. **2020**, *5*, 16987–17004.
- [17] Yao, Z.; Zhang, Z.; Liu, L.; Li, Z.; Zhou, W.; Zhao, Y.; Han, Y.; Chen, B.; Krishna, R.; Xiang, S. Extraordinary separation of acetylene-containing mixtures with microporous metal-organic frameworks with open donor sites and tunable robustness through control of the helical chain secondary building units. *Chem. Eur. J.* **2016**, *22*, 5676-5683.
- [18] Chen, K. J.; Scott, Hayley S.; Madden, David G.; Pham, T.; Kumar, A.; Bajpai, A.; Lusi, M.; Forrest, Katherine A.; Space, B.; Perry, John J.; Zaworotko, Michael J. Benchmark C₂H₂/CO₂ and CO₂/C₂H₂ separation by two closely related hybrid ultramicroporous materials. *Chem.* **2016**, *1*, 753-765.
- [19] Nugent, P.; Belmabkhout, Y.; Burd, S. D.; Cairns, A. J.; Luebke, R.; Forrest, K.; Pham, T.; Ma, S.; Space, B.; Wojtas, L.; Eddaoudi, M.; Zaworotko, M. J. Porous materials with optimal adsorption thermodynamics and kinetics for CO₂ separation. *Nature*. **2013**, *495*, 80-4.
- [20] Cadiau, A.; Belmabkhout, Y.; Adil, K.; Bhatt, P. M.; Pillai, R. S.; Shkurenko, A.; Martineau-Corcus, C.; Maurin, G.; Eddaoudi, M. Hydrolytically stable fluorinated metal-organic frameworks for energy-efficient dehydration. *Science*. **2017**, *356*, 731-735.
- [21] Mukherjee, S.; Kumar, N.; Bezrukov, A. A.; Tan, K.; Pham, T.; Forrest, K. A.; Oyekan, K. A.; Qazvini, O. T.; Madden, D. G.; Space, B.; Zaworotko, M. J. Amino-functionalised hybrid ultramicroporous materials that enable single-step ethylene purification from a ternary mixture. *Angew. Chem. Int. Ed.* **2021**, *60*, 10902-10909.
- [22] Subramanian, S.; Zaworotko, M. J. Porous Solids by Design : [Zn(4,4'-bpy)₂(SiF₆)_n·x DMF, a single framework octahedral coordination polymer with large square channel. *Angew. Chem. Int. Ed.* **1995**, *34*, 2127-2128.

- [23] Lin, M. J.; Jouaiti, A.; Kyritsakas, N.; Hosseini, M. W. Molecular tectonics: control of interpenetration in cuboid 3-D coordination networks. *CrystEngComm*. **2011**, *13*, 776-778.
- [24] Suen, M. C.; Chan, Z. K.; Chen, J. D.; Wang, J. C.; Hung, C.-H. Syntheses and structures of three new coordination polymers generated from the flexible 1,3-bis(4-pyridyl)propane ligand and zinc salts. *Polyhedron*. **2006**, *25*, 2325-2332.
- [25] Lin, M. J.; Jouaiti, A.; Pocic, D.; Kyritsakas, N.; Planeix, J. M.; Hosseini, M. W. Molecular tectonics: tubular crystals with controllable channel size and orientation. *Chem. Commun.* **2010**, *46*, 112-4.
- [26] Lin, R. B.; Li, L. B.; Wu, H.; Arman, H.; Li, B.; Lin, R. G.; Zhou, W.; Chen, B. L. Optimized separation of acetylene from carbon dioxide and ethylene in a microporous material. *J. Am. Chem. Soc.* **2017**, *139*, 8022-8028.
- [27] Wang, J.; Zhang, Y.; Zhang, P.; Hu, J.; Lin, R. B.; Deng, Q.; Zeng, Z.; Xing, H.; Deng, S.; Chen, B. Optimizing pore space for flexible-robust Metal-Organic Framework to boost trace acetylene removal. *J. Am. Chem. Soc.* **2020**, *142*, 9744-9751.
- [28] Ke, T.; Wang, Q.; Shen, J.; Zhou, J.; Bao, Z.; Yang, Q.; Ren, Q. Molecular sieving of C₂-C₃ alkene from alkyne with tuned threshold pressure in robust layered Metal-Organic Frameworks. *Angew. Chem. Int. Ed.* **2020**, *59*, 12725-12730.
- [29] Shen, J.; He, X.; Ke, T.; Krishna, R.; van Baten, J. M.; Chen, R.; Bao, Z.; Xing, H.; Dinca, M.; Zhang, Z.; Yang, Q.; Ren, Q. Simultaneous interlayer and intralayer space control in two-dimensional metal-organic frameworks for acetylene/ethylene separation. *Nat Commun.* **2020**, *11*, 6259.
- [30] M. Shivanna, K. I. Otake, B. Q. Song, L. M. van Wyk, Q. Y. Yang, N. Kumar, W. K. Feldmann, T. Pham, S. Suepaul, B. Space, L. J. Barbour, S. Kitagawa, M. Zaworotko.

Benchmark acetylene binding affinity and separation through induced fit in a flexible hybrid ultramicroporous material. *Angew. Chem. Int. Ed.* **2021**, *60*, 20383–20390.

[31] Wang, J.; Zhang, Y.; Su, Y.; Liu, X.; Zhang, P.; Lin, R. B.; Chen, S.; Deng, Q.; Zeng, Z.; Deng, S.; Chen, B. Fine pore engineering in a series of isoreticular metal-organic frameworks for efficient C₂H₂/CO₂ separation. *Nat. Commun.* **2022**, *13*, 200.

[32] Kumar, N.; Mukherjee, S.; Bezrukov, A. A.; Vandichel, M.; Shivanna, M.; Sensharma, D.; Bajpai, A.; Gascón, V.; Otake, K. i.; Kitagawa, S.; Zaworotko, M. J. A square lattice topology coordination network that exhibits highly selective C₂H₂/CO₂ separation performance. *SmartMat.* **2020**, *1*, e1008.

[33] Blochl, P. E. Projector augmented-wave method. *Phys Rev B* **1994**, *50*, 17953-17979.

[34] Kresse, G.; Furthmuller, J. Efficiency of ab-initio total energy calculations for metals and semiconductors using a plane-wave basis set. *Comput. Mater. Sci* **1996**, *6*, 15-50.

[35] Kresse, G.; Furthmuller, J. Efficient iterative schemes for ab initio total-energy calculations using a plane-wave basis set. *Phys Rev B Condens Matter* **1996**, *54*, 11169-11186.

[36] Wellendorff, J.; Lundgaard, K. T.; Møgelhøj, A.; Petzold, V.; Landis, D. D.; Nørskov, J. K.; Bligaard, T.; Jacobsen, K. W. Density functionals for surface science: Exchange-correlation model development with Bayesian error estimation. *Physical Review B* **2012**, *85*, 235149

[37] Ghysels, A.; Verstraelen, T.; Hemelsoet, K.; Waroquier, M.; Van Speybroeck, V. TAMkin: a versatile package for vibrational analysis and chemical kinetics. *J. Chem. Inf. Model.* **2010**, *50*, 1736-1750.

[38] Frenkel, D.; Smit, B. Understanding Molecular Simulation: From Algorithms to Applications. *Academic Press: New York* **2002**, 112-114.

- [39] Dubbeldam, D.; Calero, S.; Ellis, D. E.; Snurr, R. Q. RASPA: molecular simulation software for adsorption and diffusion in flexible nanoporous materials. *Mol. Simul.* **2016**, *42*, 81-101.
- [40] Dubbeldam, D.; Torres-Knoop, A.; Walton, K. S. On the inner workings of Monte Carlo codes. *Mol. Simul.* **2013**, *39*, 1253-1292.
- [41] BIOVIA, Dassault Systèmes, Material Studio, San Diego: Dassault Systèmes, 2022.
- [42] Wilmer, C. E.; Kim, K. C.; Snurr, R. Q. An Extended Charge Equilibration Method. *J Phys Chem Lett* **2012**, *3*, 2506-2511.
- [43] Rappe, A. K.; Casewit, C. J.; Colwell, K. S.; Goddard, W. A.; Skiff, W. M. Uff, a Full Periodic-Table Force-Field for Molecular Mechanics and Molecular-Dynamics Simulations. *J. Am. Chem. Soc.* **1992**, *114*, 10024-10035.
- [44] Boyd, P. G.; Moosavi, S. M.; Witman, M.; Smit, B. Force-Field Prediction of Materials Properties in Metal-Organic Frameworks. *J Phys Chem Lett* **2017**, *8*, 357-363.